



Towards an improved understanding of wildfire CO emissions: a satellite remote-sensing perspective

Debora Griffin¹, Jack Chen¹, Kerry Anderson^{1,2}, Paul Makar¹, Chris A. McLinden^{1,3}, Enrico Dammers⁴, and Andre Fogal^{1,5}

¹Air Quality Research Division, Environment and Climate Change Canada, Toronto, Ontario, Canada

²Natural Resources Canada (emeritus)

³Department of Physics and Engineering Physics, University of Saskatchewan, Saskatoon, Saskatchewan, Canada

⁴Netherlands Organisation for Applied Scientific Research (TNO), Climate Air and Sustainability (CAS), Utrecht, The Netherlands

⁵University of Waterloo, Department of Physics and Astronomy, Waterloo, Ontario, Canada

Correspondence: D. Griffin (debora.griffin@ec.gc.ca)

Abstract. Emissions from wildfires are a significant source of air pollution, which can adversely impact air quality and ecosystems thousands of kilometers downwind. These emissions can be estimated by a bottom-up approach, using inputs such fuel type, burned area, and standardized emission factors. Emissions are also commonly derived with a top-down approach, using satellite observed fire radiative power (FRP) as proxy for fuel consumption. More recently, wildfire emissions have been demonstrated to be estimated directly from satellite observations, including carbon monoxide (CO). Here, we explore the potential of satellite-derived CO emission rates from wildfires and provide new insights into the understanding of satellite-derived fire CO emissions globally, with respect to differences in regions and vegetation type. Specifically, we use the TROPOMI (Tropospheric Monitoring Instrument) high spatial-resolution satellite datasets to create a global inventory database of burning emissions CO emissions between 2019 and 2021. Our retrieval methodology includes an analysis of conditions under which emission estimates may be inaccurate and filters these accordingly. Additionally, we determine biome specific emission coefficients (emissions relative to FRP) and show how combining the satellite derived CO emissions with satellite observed FRP from the Moderate Resolution Imaging Spectrometer (MODIS) establishes an annual CO emission budget from wildfires. The resulting emissions totals are compared to other top-down and bottom-up emission inventories over the past two decades. In general, the satellite-derived emissions inventory values and bottom-up emissions inventories have similar CO emissions totals across different global regions, though the discrepancies may be large for some regions (Southern Hemisphere South America, Southern Hemisphere Africa, Southeast Asia) and for some bottom-up inventories (e.g. FINN2.5, where CO emissions are a factor of 2 to 5 higher than other inventories). Overall, these estimates can help to validate emission inventories and predictive air quality models, and help to identify limitations present in existing bottom-up emissions inventory estimates.

1 Introduction

Emissions from wildfires are a significant source of air pollution in the global atmosphere. These emissions are transported over large distances and, thus, can adversely impact air quality and ecosystems thousands of kilometers downwind (e.g., Landis



et al., 2018; Meng et al., 2019). Health impacts are typically more severe in close proximity to the fires, however health impacts from transported smoke plumes have also been reported (Matz et al., 2020). In more recent years an increase in fire activity in North America has been recorded (e.g., Romero-Lankao et al., 2014; Landis et al., 2018). The driving factors for this increase include droughts, higher temperatures, and fuel loading caused by tree death (Littell et al., 2009; Westerling, 2016). This trend may continue due to climate change (Liu et al., 2013; Wotton et al., 2017). Given the increase in fire intensity and number of fires, there is a need to accurately model and forecast smoke plumes from wildfires to be able to predict the concentration of harmful pollutants, and to issue necessary alerts on time (e.g., Yue et al., 2015). Wildfire emissions are associated with large uncertainties (Andreae, 2019), which lead to a growing demand for improved knowledge of wildfire emissions.

30

Wildfire emissions can be estimated by either a bottom-up or top-down approach. For the bottom-up estimates proxies, such as fuel type, area burned, and emission factors (EF), are used to determine the emissions; these emissions are determined by

$$E_i = \text{Activity} \times EF_{i,f}. \quad (1)$$

Where the emissions (E_i) account for mass of fuel consumed in combustion (kg), which are based on fire activity (which includes factors such as the burned area, fuel loading, fuel classification, and a combustion factor), and $EF_{i,f}$ (g/kg) is the emission factor for a specific chemical species (i), which is typically a function of fuel type (f) (sometimes it can be dependent on the combustion type as well, i.e., flaming and smoldering). An example for this type of fire emission inventory is the Fire INventory from NCAR (FINN; Wiedinmyer et al., 2011). Wildfire emissions are also commonly derived with a top-down approach, using satellite information to estimate forest fire emissions, sometimes in near-real time. The Global Fire Assimilation System (GFAS; Kaiser et al., 2012) is an example of such a system, wherein satellite observed fire radiative power (FRP, in units of W) or its time integral, fire radiative energy (FRE, in units of J) is used as a proxy for fuel consumption. Using a satellite-remote sensing FRP together with a species specific emissions coefficient (EC_i) is a common approach for top-down fire inventories: $E_i = \text{FRE} \times EC_i$. For many inventories, EC_i (in units of g/MJ) is commonly estimated from $EF_{i,f}$ (dependent on species and fuel type, in units of g/kg) and a conversion factor β_f (kg/MJ) based on fuel type (Wooster et al., 2005). The $EF_{i,j}$ is typically based on laboratory derived values and is a common factor used in both top-down and bottom-up approaches. Other inventories make use of a combination of bottom-up and top-down information (e.g. Global Fire Emissions Database (GFED; Giglio et al. (2013)). The Canadian Forest Fire Emissions Prediction System (CFFEPS; Chen et al. (2019)) and its global extension Global Forest Fire Prediction System (GFFEPS; under-development), where satellite-derived hotspot data is linked to databases such as fuel type, previous statistics on area burned per hotspot for a given fuel type, etc., to determine emissions, and may be run within an on-line air-quality model to determine the effects of fire emissions on weather (Makar et al., 2020).

Fire emission rates can also be derived directly from measurements without the proxy information of combustion processes. This is an alternative measure for evaluation of emission inventories and emission processing systems. In situ and aircraft measurements are difficult to obtain close to fires and may be rare due to the expense of observations. However, satellite-borne

55



observations provide ongoing coverage using a common instrument platform, which can thus be used to constrain wildfire emissions. Satellite-remote sensing observations also have the advantage of near-global coverage. With the recent advances in satellite observations, wildfire emissions can be estimated directly, with past work showing the utility of these observations in estimating emissions of carbon monoxide (CO) (Adams et al., 2019; Stockwell et al., 2022), carbon dioxide (CO₂) (Guo et al., 2019), nitrogen oxides (NO_x) (Jin et al., 2021; Griffin et al., 2021), and ammonia (NH₃) (Adams et al., 2019). There are several limitations to emission estimates from satellite observations: 1) direct satellite-based emissions estimates are only possible for a few chemical species that are measured by satellite instruments; 2) current satellite-based instruments are on polar-orbiting platforms that consequently only observe a location once or twice per day, a measurement frequency that will improve in the near future with new geostationary satellites; 3) many fires are missed due to cloud cover or even thick smoke that impacts the quality of the satellite observation; 4) small fires that are below the satellite detection limit will be missed.

This study focuses on deriving the emissions directly from the satellite observations. Additionally, we explore using a satellite-derived EC_i (traditionally laboratory measurements are used for EF_i and ultimately used for EC_i) for a variety of biomes around the globe. Specifically, we use the TROPOMI (Tropospheric Monitoring Instrument) high spatial-resolution satellite observations on CO and plume height information to produce biomass burning CO emission fluxes. The main advantage of the TROPOMI dataset is the wealth of observations at higher horizontal resolution (with 7 × 7 km²) compared to its predecessors (e.g., the Infrared Atmospheric Sounding Interferometer (IASI; Clerbaux et al. (2009)), and Measurement of Pollution in the Troposphere (MOPITT; Deeter et al. (2013))). Another advantage of TROPOMI over its predecessors is the high sensitivity near the surface (Schneising et al., 2020) which is beneficial when estimating emissions that occur close to the surface. TROPOMI has previously been used to estimate CO emissions from wildfires and comparisons to aircraft-derived emissions showed very good agreement for fires in North America (Stockwell et al., 2022).

The aim of this study is to establish a database of satellite-derived fire global fire CO emissions; an inventory based on satellite data alone. As we show below, this inventory provides an alternative measure that can be used to evaluate and improve fire emission inventories or fire emissions prediction systems. Additionally, we determine biome specific emission coefficients (emissions relative to FRP. We further show how combining the satellite derived CO emissions with satellite observed FRP from the Moderate Resolution Imaging Spectrometer (MODIS) can establish an annual CO emission budget from wildfires.

This paper is structured as follows: Section 2 describes the datasets and emission estimation algorithm used. Emissions from different biomes are investigated in Sect. 3. In Sect. 4 the direct estimates are compared with bottom-up and top-down fire emissions. Annual global budgets of CO fire emissions from different inventories are compared and evaluated against the satellite-derived CO emissions estimates in Sect. 5, followed by a summary and conclusions in Sect. 6.



2 Datasets and Methods

2.1 Satellite CO Dataset

The TROPOMI instrument, on-board the Copernicus Sentinel-5 Precursor (S-5P) satellite (under ESA), orbits the globe with a local overpass time of around 13:30 local time and near full-surface coverage on a daily basis (Veefkind et al., 2012; Hu et al., 2018). It has four spectrometers that cover the solar spectrum between the short-wave infra-red (SWIR) and the ultra-violet (UV). Amongst other species, total column CO is retrieved from the SWIR spectrometer at a horizontal resolution of roughly $5.5 \times 7 \text{ km}^2$ ($7 \times 7 \text{ km}^2$ prior to August 6, 2019) using the Shortwave Infrared CO Retrieval algorithm (Borsdorff et al., 2018, 2019). The TROPOMI CO columns have been validated with satellite observations (Martínez-Alonso et al., 2020), as well as with ground-based remote sensing instruments (Borsdorff et al., 2019). Both studies showed that TROPOMI exceeded its mission requirement on precision and concluded a precision error well below $<10\%$. For our analysis, we use observations with a quality flag of >0.5 (0 the lowest and 1 being the best quality), which is the recommended quality threshold (Apituley et al., 2018).

2.2 Satellite-derived CO Emissions

To determine emissions from the satellite observations, a similar approach based on Adams et al. (2019) and as described in Stockwell et al. (2022) and Griffin et al. (2021) was applied. The basic underlying concept of the method is mass balance: that the source rate Q must be equivalent to the product of the column plume transect and the wind speed (U). The mass within the box can be determined by integrating the enhanced vertical column densities (VCDs) over the background concentrations and applying the molar mass of CO. The time of a mass clearing the box is based on the length of the box and the wind speed. This methodology has been used previously to determine emissions from forest fire plumes using satellite observations (Mebust et al., 2011; Mebust and Cohen, 2014; Adams et al., 2019; Griffin et al., 2021; Stockwell et al., 2022, e.g.).

The flux methodology employed here is best applied to emitted species with slow chemical loss rates such as CO, because the flux method is insensitive to the plume shape (often the plumes are not flawless Gaussian distributions, especially for long-lived gases). Further, specifically for estimating fire emissions at a time when the fire activity is increasing (i.e. TROPOMI overpass time at 1:30 pm) will impact any attempt to estimate the chemical life-time for shorter-lived species like NO_2 (Griffin et al., 2021) from the flux method, this however will not impact the analysis for a long-lived species like CO, as the lifetime is known. The removal of the background CO is, however, very important in the flux method, and may otherwise influence the estimated emission rate significantly, as the CO background is relatively high. The grey areas in Figure 1 (a,d) thus correspond to concentrations at or below this background concentration level.

The approach described as the fitting method, is summarized here. New improvements with regards to the plume rotation and plume widths are detailed, and illustrated in Fig. 1. First, a binned upwind/downwind domain of a regular grid size ($4 \text{ km} \times 4 \text{ km}$) is established by a wind-rotation about the approximate center of the fire from the satellite observations of CO VCD (Fig.

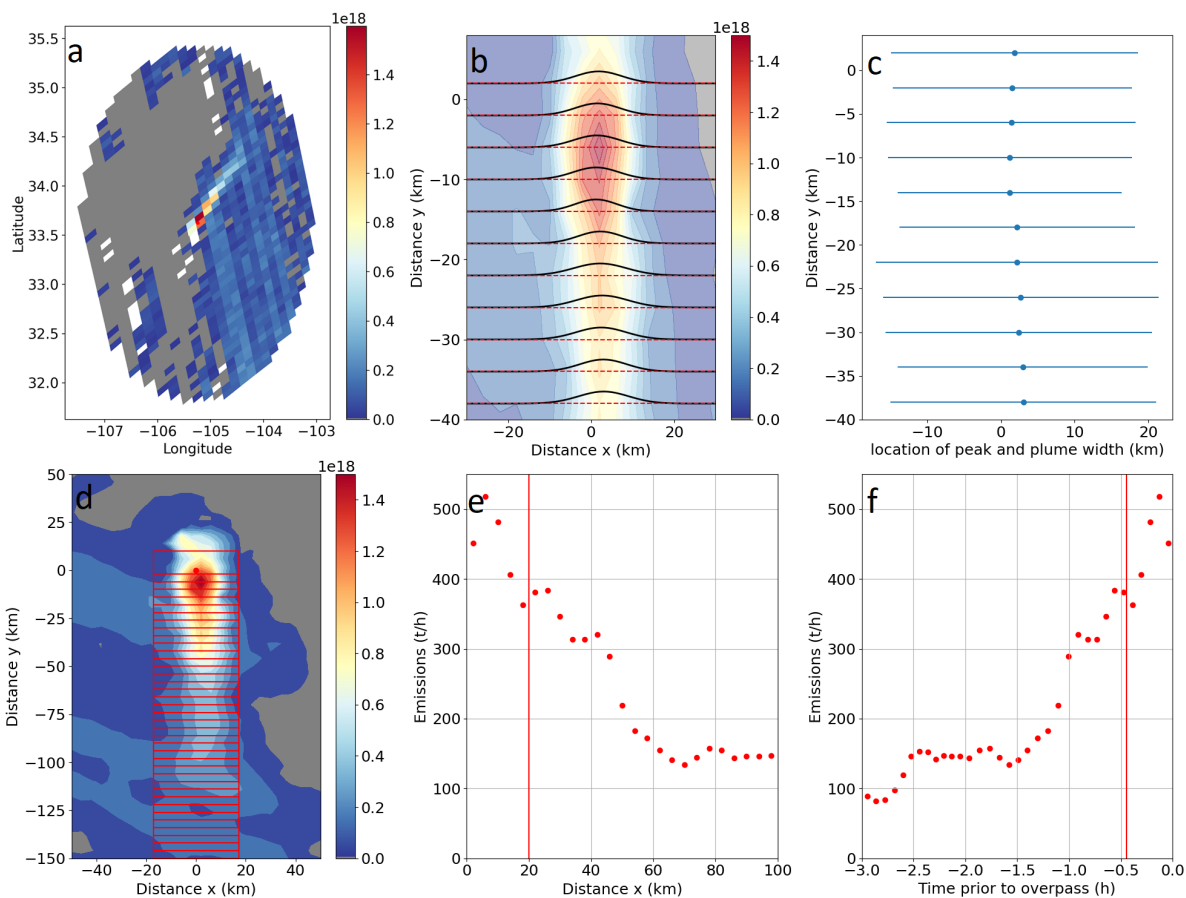


Figure 1. Illustration of the method to derive CO emissions: (a) the unmodified TROPOMI CO VCDs in a longitude-latitude domain, (b) simple Gaussians are fitted across wind in 4-km wide boxes up to 40 km downwind of the fire, (c) the peak x_0 (blue dot) and 3σ (blue bars) from the Gaussian fit are used to find the plume width and correct the wind, (d) the VCDs are rotated with the corrected wind direction and the VCDs are integrated in boxes of 4-km by 3σ , (e) the wind speed is applied to find the emission fluxes downwind of the fire, and (f) shows the same as (e) but projected in time since emissions occurred.

120 1 a). Since the grid size is slightly smaller than the TROPOMI pixels the satellite observations are weighted by the actual pixel size and over-sampled by 7 km (Adams et al., 2019). Then, along the binned VCDs, Gaussian distributions are fitted across the plume in all downwind boxes (Figs. 1 b,c), to aligned the wind direction and determine the extend of the plume. The third standard deviation out from the plume center (i.e. 99% confidence limit, Fig. 1 c) is used to define the plume lateral boundaries (typically between 10-30 km), and the wind direction correction is found by fitting a linear function through the centre of the peaks (Fig. 1 c). This new and corrected wind direction is then used to rotate the observations around the fire centre again (step 1 is repeated with the corrected wind direction). This approach is able to define the smoke plume in an automated way. A series of flux boxes of dimensions 4km in the wind direction, and 3σ in the direction perpendicular to the wind are superimposed on



the binned VCD image (Fig. 1 d). Making use of the wind fields and VCD field, the flux is then calculated (Fig. 1 e), following Mebust et al. (2011)):

$$130 \quad E_y = \sum (\Delta VCD) \times u \times A, \quad (2)$$

Where ΔVCD are the flux differences with background levels removed, u is the horizontal wind velocity, and A is the area of the box. Background CO levels are taken from averages 20 to 50 km upwind of the fire. As recommended by Griffin et al. (2021), and based on model simulation tests (in Sect. 2.3), we define the average upwind concentrations as this CO background concentration. The grey areas in Figure 1(a,d) thus correspond to concentrations at or below this background concentration
135 level.

Individual box fluxes can be used to provide estimates of the source CO emissions several hours prior to the overpass. This also provides insight into the diurnal variability of fire emissions. To be successful, meteorological conditions must have been stable several hours prior to the overpass. Figure 1 shows a very good example of such a plume for which the diurnal variability
140 could be determined; however, this is not the topic of this study, since its approach for estimating emissions several hours in the past is currently not automated or fully validated. For our final source emission estimate we use boxes within the first 20 km downwind of the fire to ensure that the time of the emission is close to the time of the overpass thus less influenced by the diurnal pattern. Since the average wind speed is roughly 20 km/h it is expected that the fire emission algorithm provides emission rates within 1 h of the overpass time. Thus, the time at which the emissions were released is expected to be approximately
145 -30 ± 30 min from the time of the TROPOMI overpass. Due to diurnal variability of fire emissions, the emissions estimate from this algorithm are time specific and do not represent a daily average. Any comparisons to emissions from other observations or inventories need to be made for the same time period. Any comparisons to emissions from other observations or inventories need to be made for the same time period.

150 For input parameters, we utilize the wind fields (U , V) from the European Centre for Medium-Range Weather Forecasts (ECMWF) ERA5 reanalysis dataset at a resolution of $0.25^\circ \times 0.25^\circ$ with an hourly output, between 1000 and 300 hPa at a resolution of 50 hPa, and interpolated spatio-temporally to the TROPOMI observations. For large fires, the rotation of observations around a single point will cause imperfections, as they are not true point sources but are spread over large areas. However, the flux methodology captures the width of the plume in these cases, with the main effect the addition of some variability in
155 the emissions at the first box of the overpass. To find the appropriate wind speed to use for emission transport, we use the average TROPOMI aerosol height (AER_LH) for each fire, which is a good proxy for the average height of fire plumes (Griffin et al., 2019). If there are no good quality plume heights near the fire, we use 2 km (or 800 hPa) (Griffin et al., 2020) for the plume height. This approach to find appropriate altitudes for wind fields has previously been successfully used to improve the accuracy of satellite-derived NO_x emissions from wildfires (Griffin et al., 2021).

160

As this method assumes steady state and relies on stable meteorology appropriate quality criteria need to be applied to fil-



ter any cases when the emission estimate might be deficient. The quality criteria to filter emission estimates as well as the total uncertainty of the emission estimates are further examined in the next section.

2.3 Accuracy of the emission estimates using synthetic data

165 Similar to Griffin et al. (2021), we conducted a sensitivity test using a regional air-quality model to create synthetic CO VCDs. Applying the fitting method used for satellite observations (as described in the previous section), source emissions retrieved from plumes generated within a model domain can then be compared directed to the original source emissions used by the model. For these tests all emissions are known, thus allowing us to: 1) test if the fitting method is able to regenerate the original emissions; 2) obtain a better idea of the uncertainties of the method; and 3) examine the extent to which quality filters should
170 be applied to the satellite-derived emissions. For this sensitivity test, we use the Global Environmental Multiscale - Modelling Air-quality and CHemistry (GEM-MACH; Makar et al. (2015b, a); Chen et al. (2019)) air quality model to obtain the synthetic VCDs. The operational version of GEM-MACH that employs forest fire emissions using CFFEPS (Chen et al., 2019), was used. This has a $10 \times 10 \text{ km}^2$ grid cell size for the North American domain, and 80 vertical levels (from the surface to approximately 0.1 hPa), further details can be found in Makar et al. (2015b, a). Although GEM-MACH's resolution is coarser than the 4 km
175 pixel size used here, the higher pixel resolution becomes available as the pixels are binned using a distance weighted average. GEM-MACH provides hourly output, with an internal "physics" time step of 7.5 min. The meteorological component of GEM-MACH is within the physics module of the Global Environmental Multiscale (GEM) weather forecast model (Côté et al., 1998; Girard et al., 2014). GEM-MACH contains a detailed atmospheric chemistry scheme, which includes the emission and removal processes of 42 gaseous species and 8 particle species. The operational model run is initialized every 12 hours, at 00 and 12
180 UTC. Original input fire emissions are estimated based on hotspot location using the CFFEPS (Chen et al., 2019)), which links the hotspot locations to ecozone-specific databases of fire area per hotspot per unit time, fire stage (crown, duff layer, residual), and estimates plume height using plume rise calculations based on meteorological lapse rates and similar considerations. For a time period between May to September 2019, the model CO profiles are integrated over the first 39 layers (approximately the lowest 10 km of the atmosphere) to obtain VCDs over the model domain, in North America (Canada and US). The wind
185 speed and wind direction used in this sensitivity test are based on forecast winds that drive the model simulations. The wind altitude for the synthetic retrieval is from the nearest model wind level to the predicted the aerosol layer peak concentration. For this time period (May to September 2019, in the US and Canada) a total emissions of 208 fires were "successfully" retrieved (a solution was found by the fitting algorithm). The results of all the retrieved emissions using the GEM-MACH output at 20UTC versus the original (synthetic) source are illustrated in Fig. 2 a. Many of the retrieved emissions are very close to
190 the original emissions, however, many outliers can be seen, where most likely the retrieved values are below the originals. An underlying requirement of the fitting methodology is the assumption that a steady-state in the meteorological conditions has been maintained during the time of the retrieval – previous work has shown that when this assumption is incorrect, the retrieved emissions may be in error (Fathi et al., 2021). Changes in meteorological state during the retrieval period (such as a change in wind direction or speed, changes in atmospheric stability) may influence retrieval accuracy, as may the presence of



195 other sources nearby to the fire of interest. Examining these cases more closely we identified certain unfavorable conditions as follows (the filtered values due to these specific conditions are illustrated in Fig. 2:

1. The background (“B”) is too high ($>0.7 \times 10^{19}$ molec/cm²): this indicates potentially upwind sources, of large enough magnitude that the plume may be difficult to distinguish, or a misplacement of the fire centre, and thus these cases should be filtered (two estimates were filtered that way).

200 2. The variation in the wind direction (“wd”) should to be less than 15°: changes in wind direction during the retrieval allow for potential convergence / divergence to occur within the model grid cell, violating the requirement of steady-state flow (78 estimates were filtered that way).

3. The plume width (“width”) should be no larger than 50 km: the method cannot be used for very large fires, as the assumption of a point source breaks down; a width larger than 50 km could also be associated with interference from
205 other nearby other sources (five estimates were filtered that way).

4. The difference of the emissions from individual cross-sections (Δ xsect) considered for the estimate (within 20 km of the fire) should be no larger than 100 %, and cases are also filtered where only one cross-section is used for the estimate: cases with high variability of the individual cross-sections indicate high variability of emissions within a very short time frame or unstable conditions (30 estimates were filtered that way).

210 Other parameters were also tested but were not included as part of the quality filter, such as variation in wind speed, maximum and minimum wind speed, height of the aerosol layer, the Richardson number and the wind shear. It should be noted that for all cases the minimum wind speed was above 2 m/s and the maximum wind speed was 11 m/s. We would expect that the method is not reliable for very high or very low wind speeds (approximately >2 m/s), as found by other studies (e.g. de Foy et al., 2014). After applying the quality filter (black points in Fig. 2) 105 fires remain (some filters overlap). The correlation is high
215 between the retrieved and original source emissions with $R = 0.92$ and a slope of best-fit (using geometrical mean) of 1.1. The relative difference is 34 % (fitted-input) which is used in our uncertainty analysis (Table 1).

The four established quality controls noted above were then used to filter the satellite-derived emissions estimates, and are recommended in retrievals of this nature. In addition, for the satellite-derived emissions, a filter that requires at least five obser-
220 vations for the estimate has also been applied. These tests using synthetic data can also help to establish the uncertainties for the estimated emissions. The total uncertainty of the satellite-derived emissions (see Table 1), is based on the uncertainty of the satellite VCDs (10 % (Sha et al., 2021)), uncertainties of the wind speed (≈ 10 %), the effect of the altitude used for the wind speed (≈ 20 %), and the uncertainty of the method itself (based on the relative difference between the true and fitted emis-
225 sions of 34 % after applying the above mentioned quality filters). The uncertainty of the wind speed caused by the uncertain altitude of the plume is based on the mean difference of the wind speed when comparing the winds 50 hPa above and below the aerosol layer height. These errors are added in quadrature, leading to a total uncertainty of approximately 42 %. The uncertainty of the wind speed is based on Gualtieri (2022) who found approximately 0.5 m/s for the 90 % confidence interval for



Table 1. Summary of uncertainties for the satellite emission estimates.

Type	Uncertainty
Satellite VCDs	3-10 %*
Method	34 %
Wind	10 %**
Wind altitude	20 %
Total	40-42 %

*Sha et al. (2021), **Gualtieri (2022)

ERA5, with the average wind speed of approximately 5 m/s (for our dataset), we assume a 10 % uncertainty for the wind speed.

230 Overall, the sensitivity tests suggest that the fitting method is robust once filters have been applied to ensure that the underlying assumptions of steady-state meteorological conditions is maintained for the observed data, and can be used to estimate the CO fire emissions. The total uncertainty of the CO emission estimates (after the above mentioned filters have been applied) is approximately 42% based on the uncertainty of the wind speed, CO VCDs and methodology. Throughout Sects. 4 and 3 these same filters that ensure steady-state meteorological conditions and low interference from nearby sources were applied to the
 235 satellite-derived emission estimates.

2.4 Satellite FRP and Hotspot Identification

To find the locations of fires around the globe we use MODIS instrument thermal anomalies and FRP products. MODIS was used in this study for two purposes: (1) to obtain the fire locations and fire centres using MODIS thermal anomalies that are then used to attempt deriving CO emissions from TROPOMI; (2) to obtain the FRP for each fire to determine the emissions
 240 coefficient (EC; see Sect. 4). The MODIS instruments, on board the NASA Earth Observation System Terra and Aqua satellites, detect fires using data collected in the infrared and spectral channels (Kaufman et al., 1998). Typical overpass times occur at approximately 10:30 AM/PM and 1:30 AM/PM local time for the TERRA and AQUA platforms of which MODIS is a component, respectively.

245 The MODIS thermal anomaly product (MOD14) (Giglio et al., 2003, 2006, 2016) from Aqua (13:30 local time) is used in this study to locate the forest fires. These thermal anomalies are clustered, with the criterion of a minimum summed FRP (within a 5 km radius) of 1000 MJ/s and a confidence of at least 75 %. These thresholds have been applied to remove fire that are too small, as the TROPOMI CO emission estimate very likely fails for very small hotspots and to reduce the influence of other (smaller) sources causing thermal anomalies (e.g. flares). Again, we would like to highlight that not all fires are captured
 250 by satellites (including MODIS), fires can potentially be missed for several reasons: if the FRP signal is too low (e.g. small fires), due to cloud cover, and under thick smoke plumes. These locations are used to attempt a CO emission estimate with

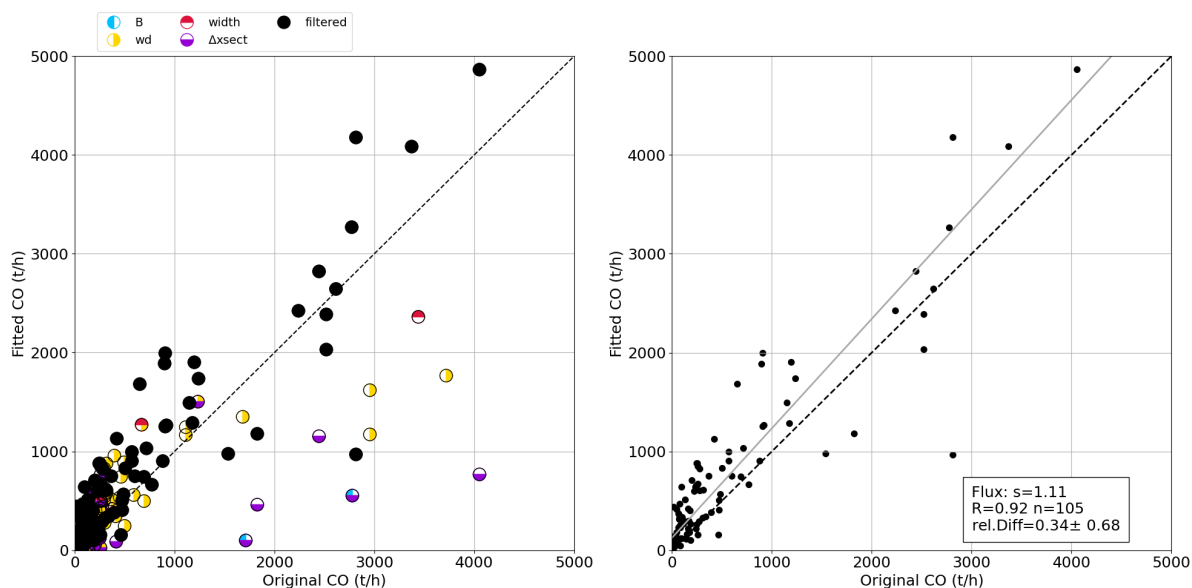


Figure 2. The results of the sensitivity test with synthetic VCDs are illustrated (see text for additional details). The filtering low quality results are illustrated in panel (a), where different parameters have been tested, including the maximum value of the background (“B”), the deviation of the wind direction (“wd”), the maximum width of the plume (“width”), and the difference between the individual cross-sections (“ Δx_{sect} ”). The filtered fitted emissions versus the model input emissions are plotted in panel (b) together with the statistics (slope of best-fit using the geometric mean, s ; correlation coefficient, R ; the number of points, n ; and the mean and standard deviation of the relative difference, $rel. Diff$: fitted-input).

TROPOMI, however, it is not always possible to derive emissions from the fire hotspot location and many locations will fail or are filtered (as mentioned in Sect. 2.3) after the emission estimate. The most common reasons for failed emission estimates include variables winds, low CO columns that are too close to the background concentrations, nearby CO sources (such as a second fire plume), and cloud cover.

MODIS FRP has also been used to estimate the emission budget, presented in Sects. 3 and 5. For the CO emission budget we use our estimated EC_{CO} (Sect. 4) and apply these to the assimilated daily GFAS FRP on a $0.1 \times 0.1^\circ$ grid to estimate a global budget of CO emissions. GFAS is a top-down emission estimation system from ECMWF. The GFAS assimilated FRP is based on the MODIS Aqua and Terra FRP that provide typically one daytime and one nighttime overpass each. This dataset provides a guidance on total daily FRP that can then be combined with the derived ratio between TROPOMI CO emissions and MODIS FRP. Since TROPOMI only provides an emission estimate around 1:30PM (local time) accounting for diurnal variability is not feasible with TROPOMI alone. Thus, a secondary dataset such as MODIS, with multiple overpasses per day at various times, is necessary to get an approximation and of diurnal fire activity and ultimately to obtain a total emission budget. This emission budget is used in Sect. 5 to compare the here estimated CO emissions with fire emission inventories. It should be noted that



some smaller fires might be below the MODIS detection limit, and will be missed and in the presence of clouds or thick smoke the instruments may not be able to observe the Earth's surface. The retrieved emissions generated here may therefore be lower limits.

2.5 GFFEPS

270 We compare our retrieved CO emissions to several existing biomass burning CO inventories and emissions estimation methodologies, as noted above, including a new global biomass burning algorithm, GFFEPS, described here. GFFEPS is a global extension of the CFFEPS model described in Chen et al. (2019). Similar to CFFEPS, GFFEPS is a bottom-up approach utilizing satellite-detected hotspots to calculate smoke emissions. The model uses the Visible Infrared Imaging Radiometer Suite (VIIRS) that then predicts emissions based on the Canadian Forest Fire Danger Rating System (CFFDRS, Stocks et al. (1989)).

275 Fuel types were assigned using the Global Land Cover (GLC) 2000 (European Commission, 2003). Area burned per hotspot was estimated based on eight years of satellite hotspot data (2012-2019) and reported area-burned statistics for the same time periods and locations using MCD64CMQ (Giglio et al., 2020). Daily fire weather conditions based on the Canadian Forest Fire Weather Index (FWI) System (van Wagner, 1987) were calculated in the global version of ECCC's Global Environmental Multiscale (GEM) model (Côté et al., 1998) and interpolated to hotspot locations. Fire behaviour conditions at each hotspot

280 were based on the Canadian Forest Fire Behaviour (FBP) System (Forestry Canada Fire Danger Group, 1992) and calculated in the Canadian Wildland Fire Information System (Lee et al., 2002) operated by the Canadian Forest Service, Natural Resources Canada (<https://cwfis.cfs.nrcan.gc.ca/>; last access: Feb. 7, 2023). Surface and crown fuel consumption rates are translated directly into smoke emissions. Emissions rates per species per stage of combustion are based on Urbanski (2014). A fix diurnal profile is applied to the daily estimated burn area to obtain an hourly fraction with peak activity at 5 pm local time. Note that

285 assignment of GLC 2000 land classifications to Canadian Fuel types and adjustments to fit global conditions continues to be an area of development in the model. Fuel loads were largely taken from van Leeuwen et al. (2014) and van der Werf et al. (2017) as used in GFED.

3 Evaluation of direct vs bottom-up emissions

CO fire emission can be estimated from TROPOMI single overpass observations. Stockwell et al. (2022) have shown when

290 comparing satellite derived CO fire emissions to aircraft derived fire emissions from measurements as part of the FIREX-AQ campaign (Warneke et al., 2023) in the US. Sensitivity tests in Sect. 2.3 also suggest that emissions can be reliably estimated using the flux method within 42 % uncertainty. In this section, TROPOMI-derived emission estimates are used to evaluate the GFFEPS emissions processing system. Figure 3 shows an example of a fire in Arizona on June 21, 2019 in the Temperate Forest North America (TENA) region (33.5°N, 111.14°W). GFFEPS emissions are given in 3 h intervals and shown as orange

295 dots. GFFEPS estimates daily emissions based on area burned, and utilizes a prescribed diurnal pattern with a peak in fire intensity and emissions in the late afternoon. The peak in emissions always occurs a few hours after the TROPOMI overpass. TROPOMI overpass time was around 20:30 UTC and the emission estimate is shown as a black triangle. The GFFEPS emis-

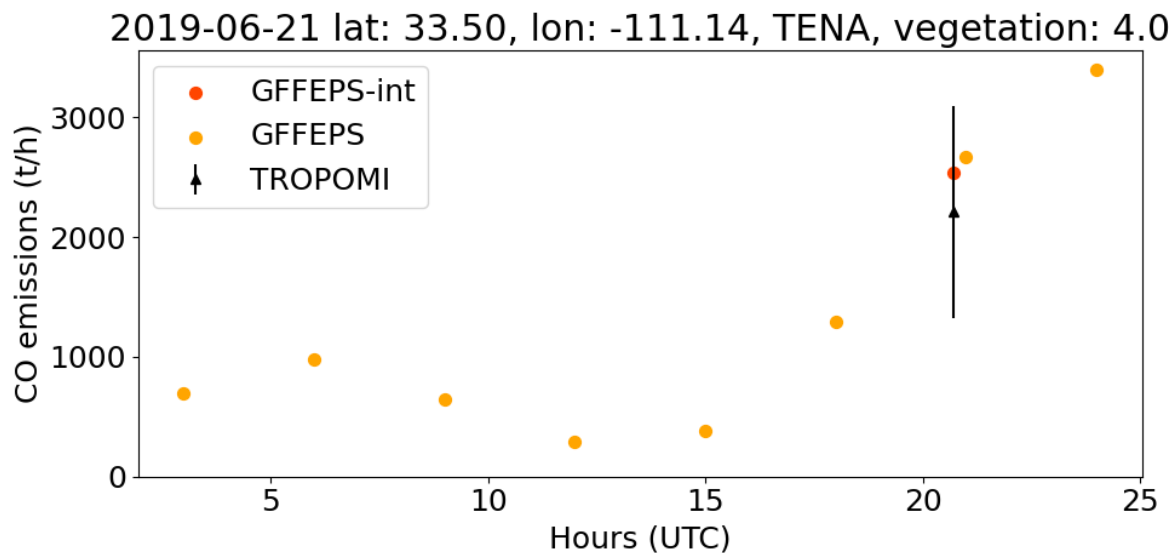


Figure 3. Comparison between TROPOMI-derived CO (black triangle), and GFFEPS (yellow) CO emissions on the example of a fire in Arizona, US (TENA, 33.5°N, 111.14°W) on 21 June 2019. Also shown are the time-interpolated GFFEPS emissions to the time of the TROPOMI overpass (red, “GFFEPS-int”).

sions are interpolated to the TROPOMI overpass time (shown as a red dot), and for this example GFFEPS aligns with the satellite-derived emissions very well.

300 The TROPOMI-derived emissions can be used more broadly to examine the performance of the GFFEPS emissions. Figure 4 (a) shows the comparison between TROPOMI and GFFEPS (at the overpass time of TROPOMI, equivalent to the orange dot in Fig 3) for roughly 5000 fires globally in 2019 (all fires where TROPOMI could successfully estimate CO fire emissions, appropriate filters as described in Sect. 2.3 have been applied). The results show that the model captures the order of magnitude and some of the variability, however, on average GFFEPS tends to predict lower emissions than the satellite-derived CO emissions.

305 The cause for this bias is being investigated; possible reasons for this could be the following: 1) misrepresentation of fuel type and/or its associated emissions factors; 2) the estimated area burned could be incorrect; 3) the diurnal variability is not accurately represented; or 4) the time assumed for the TROPOMI-derived emissions is not correctly represented. To examine the reasons more closely and to pinpoint the issues, specific areas and fuel types were examined individually (see Tables A1 and A2). This shows that for certain regions (i.e. CEAM, NHSA, EURO, and MIDE) the model agrees pretty well with the satellite-derived emissions (taking slope, R and RMSE into consideration).

310 Other regions, like AUST have a very poor correlation, slope and RMSE, indicating a need to improve the modelling of that region. In terms of biomes (see Table A2, the results are less clear, as biome 1 dominates the AUST region for fires in 2019 and also shows a very poor correlation.



We also examine individual fires contributing to this issue in Figure 5 which depicts an example of a fire where the GF-
315 FEPS and TROPOMI values compare well (top row of panels) and a fire where the GFFEPS values are much lower than the
satellite observations. Shown are the TROPOMI CO VCDs (Figs. 5 a and d), the GEM-MACH VCDs (using GFFEPS emis-
sions) in Figs. 5 b and e, and the true color image together with the MODIS hotspots (Figs. 5 c and f). The fires that tend to
underestimate the directly-derived CO emissions significantly are predominantly the ones that are influenced by thick smoke
(and/or clouds). Some of the lower emissions from GFFEPS may suggest that fires emitting thick smoke may have underes-
320 timated hotspot values – a correction for fires influenced by thick smoke reducing the number of observable hotspots may be
necessary.

Specifically at the overpass time, the emissions are often underestimated by GFFEPS when comparing individual fires (at the
time of the TROPOMI overpass). The TROPOMI overpass time (1:30 pm local time) is exactly at a time when fires typically
325 experience significant growth, one or two hours either side of the overpass time make a difference of approximately 30-50 %
(see Fig. 3). Thus, the lower emissions could also be the result of a timing issue, either from GFFEPS or the time assumed for
the TROPOMI-derived emissions. GFFEPS prescribes a diurnal emission profile, whereas the TROPOMI emissions provide
an emission rate specific to a satellite overpass time. As can be seen in Fig. 3, the diurnal variation in GFFEPS emissions can
be substantial. While the satellite data only allows evaluation of GFFEPS at the overpass time (and hence an evaluation over
330 all times of emissions is not possible). We can conclude that model emissions (specifically at the overpass time) capture at
least some of the variation in CO emissions at overpass time ($R = 0.22$), but are general biased low compared to the satellite
derived emissions in the early afternoon. The total daily emissions and the diurnal variability are still a large uncertainty, and
cannot be readily evaluated using polar orbiting satellites such as TROPOMI (since TROPOMI can only provide limited times
to obtain CO fire emissions).

335

Overall, TROPOMI CO emission estimates can be used to help with the evaluation of the emission model and help pinpoint
certain areas that need further improvement.

4 Emission Coefficients for Different Vegetation Types from Satellite-Derived Emissions

Annual CO emissions can be estimated based on TROPOMI and MODIS FRP observations. Emission coefficients, here de-
340 fined as the ratio between the TROPOMI-derived CO emissions and MODIS FRP, are used to obtain an annual emission budget
by region. Emission inventories can then be compared to study trends over time (see Sect. 5). The emission coefficients can
also provide information on the burning efficiency of different vegetation types. The TROPOMI-derived CO emissions alone
cannot be used to obtain annual total emissions because: 1) emissions of many fires will not be possible to be derived directly
(e.g. due to unfavorable meteorology, cloud cover, size of the fire etc.); and 2) TROPOMI is in a low earth orbit observing
345 each location once or twice per day and the TROPOMI-derived emissions are limited to the time of these overpasses. The
emissions coefficients can be determined from the correlation and slope of best-fit between the CO emissions and coincident

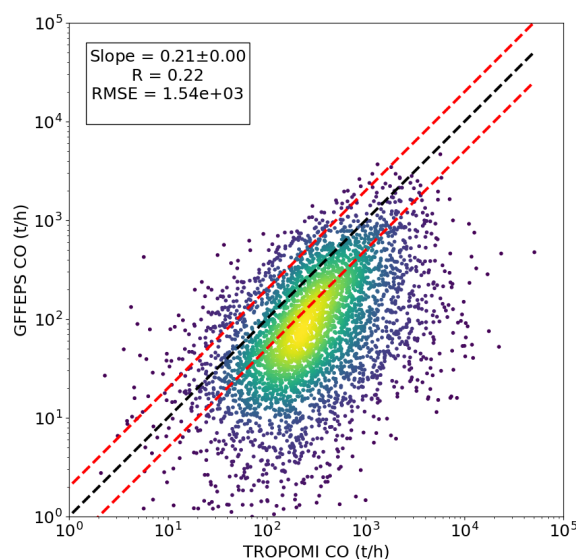


Figure 4. Comparison between approximately 4000 TROPOMI-derived CO emissions and (a) GFFEPS for 2019 fires. The colours indicate the density of the points (yellow being high density and blue being outliers). Note that the axis are in logarithmic scale, showing the 1-to-1 line (black) and the 1-to-2 lines (red). GFFEPS tends to be lower than the directly-derived TROPOMI emissions.

FRP observations (Mebust et al., 2011; Mebust and Cohen, 2014; Adams et al., 2019).

Emissions factors will change with different stages of a fire (flaming to smoldering); however, it is challenging to separate
 350 the different burning stages from fires (Andreae, 2019). For the emission coefficients derived in this study we did not separate
 the burning stages; instead, a single emission coefficient is used for each biome for the following reasons: 1) The MODIS-based
 GFAS FRE (total daily FRP) is a binned product, trying to project any assumptions of burning stages will introduce more un-
 certainty; 2) fires will most likely be flaming at the time of the TROPOMI overpass (1:30 pm local time). It is likely that these
 different burning stages have different CO emission coefficients (EC). For example, Hayden et al. (2022) identified that the CO
 355 EC is almost twice that during smoldering compared to flaming (this does not mean that emissions might be underestimated
 by the same amount, the FRP is significantly lower during smoldering stages and thus reduces the induced error). In that case
 study it was possible to roughly differentiate between smoldering and flaming; however, for large sample of fires it is very
 difficult to do so. The point is, that a mix of flaming and smoldering fires will reduce the correlation coefficient (e.g. Fig. 6),
 the overall EC will result in an average of flaming and smoldering EC. When applying these ratios globally to binned MODIS
 360 FRE to obtain annual emissions it is likely to average out overall, but all information on smoldering and flaming is lost in these
 averages. It is the norm for top-down inventories to apply a single emission coefficient (per vegetation) that does not change
 with the time of day (e.g. GFAS).

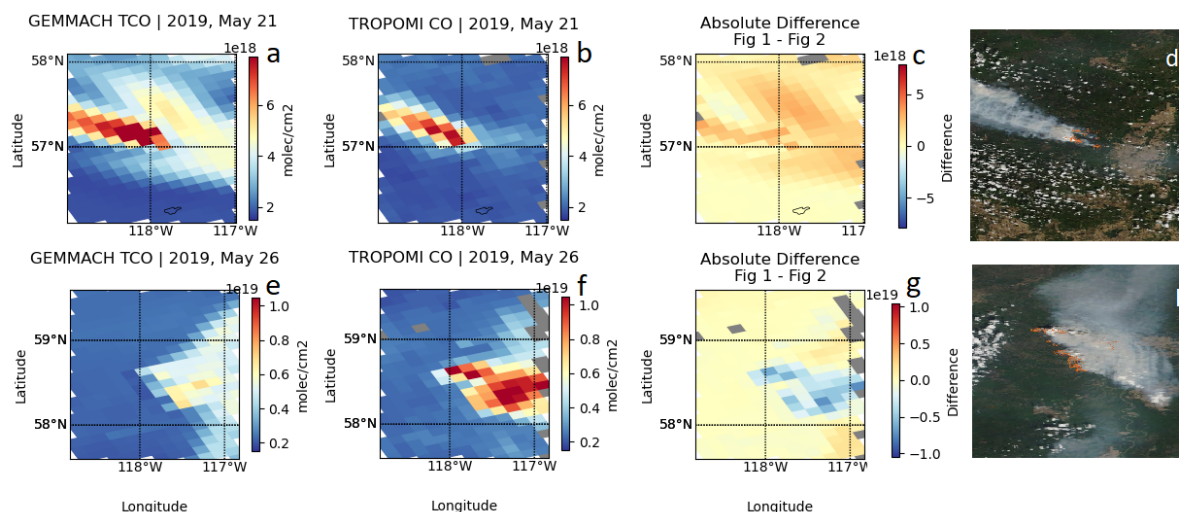


Figure 5. Comparison between model and TROPOMI-observed CO VCDs for two different fires. Top shows an example of a good match between the model (a) and TROPOMI (b), where the model input emissions (GFFEPS) are similar to the satellite-derived emissions. The difference (model–TROPOMI) can be seen in (c). (d) shows the VIIRS true color image for the same scene together with the day time MODIS thermal anomalies (hotspots, red dots), obtained from NASA Worldview; <https://worldview.earthdata.nasa.gov/>. The bottom figures show an example of a bad match between the model (e) and TROPOMI (f), where the model input emissions (GFFEPS) are significantly lower, with the difference shown in (g) and the VIIRS true color image in (h).

To differentiate biomass burning emissions in different biomes we use the GLC2000 (European Commission, 2003). This
 365 land use classification dataset distinguishes between 22 different types of biomes. A full list can be found in the Appendix,
 Table B1. In summary: 1-10 are different types of forests; 11-12 are types of shrub; 13-15 different types of grassland (herba-
 ceous cover); 16-18 different types of Mosaic (cultivated areas and crops); 19-22 are areas where fires are unlikely (including
 water, snow, and urban areas). From the 22 possible types of biomes, we include a total of 15 different biomes in our analysis,
 excluded are biomes where fires were not observed, namely: regularly flooded tree cover (7 and 8), previously burned tree
 370 cover (10), bare areas (19), water bodies (20), snow and ice (21), and artificial surfaces (22).

Figure 6 shows the correlation between the TROPOMI-derived CO emissions (2019-2021) and the total MODIS Aqua FRP
 (which has a similar orbit as TROPOMI) for the corresponding fire for Tree Cover, broadleaved, evergreen (biome 1). The
 slope between the CO emissions (in g/s) and the FRP (in MJ/s) is EC (in g/MJ), the values of which are shown in Table 2.
 375 A geometric mean approach was used to find the slope of best fit and the 99 % confidence level (used as the uncertainty of
 the EC). The results for all biomes used in the analysis are summarized in Table 2. The sample size specifies the number of
 fires used for the regression analysis and the rank is number of importance with respect to the total annual FRP from GFAS
 (for the 2019 base year). The total FRP identifies how much each of these different biomes contribute to the total annual

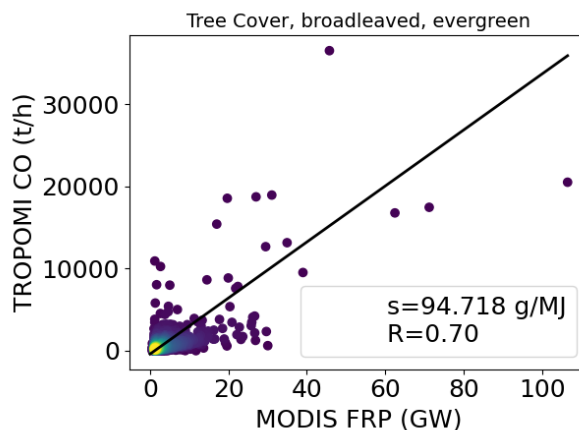


Figure 6. TROPOMI-derived CO emissions (2019-2021) versus MODIS detected FRP for fires from broadleaved evergreen trees. The color indicates the density (yellow being the most dense and blue being the outliers) of the 842 fires.

budget (Sect. 5). The emission coefficients vary between 120 and 39 g/MJ, where the largest CO emissions relative to FRP
380 are from broadleaved evergreen tree cover (1) and the lowest are from cultivated managed areas (16). Correlation coefficients
vary significantly for different biomes. Most biomes have a moderate to high correlation with a correlation coefficient that is
between approximately 0.5-0.9. The lowest correlation coefficient ($R = 0.34$) is found for Mosaic: Cropland / Tree Cover /
Other natural vegetation (biome 17) meaning that the CO emissions are quite variable. A simplified classification of forest,
shrub and grassland did not lead to better results. For example the EC_{CO} for different types of forests vary between roughly
385 49 and 95 g/MJ. An attempt was made to simplify the biomes following the approach of Mebust et al. (2011); however, this
depreciated the correlation coefficients significantly. Based on the 22 biomes used here suggests additional subclassification of
biomes might be necessary to further improve the correlations used to estimate EC_{CO} values across different parts of the globe
(e.g., the CFFDRS has seven classifications for coniferous forests, here described as biome 4). There are certain advantages
to combining the TROPOMI-derived ECs for CO and the MODIS FRP. It is possible with this approach to obtain a budget of
390 annual (or monthly) CO emissions from wild fires, because of the more continuous and diurnal coverage of MODIS FRP with
at least 4 overpasses at various times during day and night (GFAS FRP). This can then be used to make a comparison between
emission inventories and TROPOMI derived CO. There is also the potential to apply these ECs to other years (even before the
launch of TROPOMI), the following section will discuss this in more detail.

5 Global CO Budget

395 Applying TROPOMI-MODIS-derived ECs to daily integrated MODIS FRE (that captures the diurnal fire activity) can help to
analyse the CO emission budget and can allow to compare it to existing fire emission inventories. The ECs (derived in Sect.
4) are here applied to the daily GFAS FRP, assimilated FRP observations from the Terra MODIS and Aqua MODIS satellite



Table 2. Emissions coefficients for CO (EC_{CO}) \pm the 99 % confidence interval (note this is only a mathematical error for the determination of the slope), correlation coefficient (R), number of fires (sample size) and rank of importance in terms of total FRP (“Rank”) derived from TROPOMI and MODIS FRP for fires globally between 2019 and 2021. The biome definition is taken from GLC2000, see Table B1.

Number	Description	EC_{CO} (g/MJ)	R	sample size	Rank
1	Tree Cover, broadleaved, evergreen	95 \pm 5	0.70	842	1
2	Tree Cover, broadleaved, deciduous, closed	86 \pm 7	0.51	425	4
3	Tree Cover, broadleaved, deciduous, open	64 \pm 5	0.38	667	2
4	Tree Cover, needle-leaved, evergreen	59 \pm 7	0.48	442	8
5	Tree Cover, needle-leaved, deciduous	93 \pm 6	0.52	1040	10
6	Tree Cover, mixed leaf type	49 \pm 22	0.52	26	15
9	Mosaic: Tree cover / Other natural vegetation	63 \pm 9	0.68	111	12
11	Shrub Cover, closed-open, evergreen	120 \pm 20	0.50	162	13
12	Shrub Cover, closed-open, deciduous	39 \pm 2	0.68	465	3
13	Herbaceous Cover, closed-open	40 \pm 4	0.47	283	6
14	Sparse Herbaceous or sparse Shrub Cover	81 \pm 17	0.53	72	9
15	Regularly flooded Shrub and/or Herbaceous Cover	105 \pm 17	0.62	127	14
16	Cultivated and managed areas	62 \pm 7	0.59	250	5
17	Mosaic: Cropland / Tree Cover / Other natural vegetation	67 \pm 13	0.34	111	7
18	Mosaic: Cropland / Shrub or Grass Cover	61 \pm 5	0.87	129	11

sensors. The domain is global with a resolution of 0.1° on a regular latitude-longitude grid. The time period between 2003 and the present is covered. The resulting top-down emissions, referred to as “TROPOMI/FRE”, can be used to study the distribution of fire emissions more generically. Figure 7 shows the distribution of the CO emissions for 2019 by (a) biome, (b) region, and (c) month. Most CO emissions are from evergreen forests (biome type 1), which also has the largest EC for CO (see Table 2). About two thirds of wildfire CO emissions are from forests (type 1-6). The regions affected by the largest CO fire emissions are Southern Hemisphere Africa (SHAF, 25 %) and Southern Hemisphere South America (SHSA, 20 %). The least affected are Europe (EURO) and the Middle East (MIDE), these regions have the least amount of fires and the smallest wildfire CO emissions, below 1 % of the global emissions. The annual cycle is a little more evenly distributed with emissions between roughly 5-15 %, and shows the peak of CO emissions in August (15 %) with the lowest emissions in May (4.5 %). It should be noted that 2019 was an unusual year for Australia with high intensity fires in December 2019 (during the 2019/2020 Australian summer), also known as the “black summer” (e.g. van der Velde et al., 2021; Pope et al., 2021). These fires contributed significantly to the global December emissions (Fig. 7 (c)). The type of biome burned was Eucalyptus forest, which is classified as biome 1.



The total wildfire related CO emissions using TROPOMI/FRE are approximately 288 Mt in 2019. The total from TROPOMI/FRE may be compared to those from other fire emission inventories: GFFEPS (337 Mt), the top-down inventory GFAS (364 Mt), the bottom-up inventories: GFED (408 Mt), FINN v1.5 (295 Mt), and FINN v2.5 (579 Mt). The break-down for 14 common geographical regions around the globe, as defined by (Giglio et al., 2013, Fig. 1), can be seen in Fig. 8. Even though the here presented TROPOMI/FRE product is based on GFAS FRP, there are significant differences between these two data sets. Most noticeable in the Equatorial Asia (EQAS) and Boreal Asia (BOAS) region where TROPOMI/FRE is significantly lower and the Southern Hemisphere Africa (SHAF) region where it is higher. FINN v2.5 stands out as the fire emission inventory with the highest emissions, almost twice as large as FINN v1.5. FINN v2.5 emissions are especially high for Southeast Asia (SEAS). The inventories show consistently the largest CO emissions due to wildfires from SHSA and SHAF (with most fires just south of the equator), a result of the Amazon tropical forest fires and Congo's forested ecosystem, respectively. For Boreal North America (BONA), Temperate North America (TENA), Central America (CEAM), Northern Hemisphere South America (NHSA), Europe (EURO), Middle East (MIDE), Northern Hemisphere Africa (NHAF), and Centraleast Asia (CEAS), there is agreement within a factor of 2 (but often better than that) between the different inventories. EQAS and BOAS are the regions where CO emissions seem quite uncertain and are the least consistent between the different inventories with rates between approximately 10-80 and 10-70 Mt for 2019, respectively. The most noticeable differences are for FINN v1.5 and v2.5 that are exceptionally high in the SEAS region compared to all other estimates. CO emissions from EQAS and BOAS seem high for the GFED and GFAS estimates compared to the other inventories. BONA CO emissions are also about twice as high for GFED and GFAS compared to the other estimates. Australia (AUST) is very low for FINN v1.5 (roughly a factor of 5) compared to the others. The low bias in GFFEPS (as found in Sect. 3) cannot be seen in this comparison. One possibility is that the bias seen in the previous section is due to an inaccurate diurnal pattern, but there could be other reasons too. To be certain, further investigation is required that is outside the scope of this study. Overall, Fig. 8 highlights that there are large discrepancies especially for certain regions around the globe with regards to wildfire related (CO) emissions. Using a measurement based approach can help with the evaluation of the different inventories, as was done in Sect. 3 for individual fires. Again, it should be highlighted that all these top-down and bottom-up inventories rely to a certain extent on good coverage of hotspot locations. If the fire hotspots cannot be measured by MODIS (due to clouds or thick smoke) the emissions will be underestimated, which is a difficult bias to properly correct for without introducing further assumptions and uncertainties. If anything, the true CO wildfire emissions are likely higher than the ones here presented, due to missed fire hotspots and the underestimate of large fires (with thick smoke).

5.1 CO emissions over the past two decades

GFAS FRP, based on MODIS FRP, is available from 2003 to the present. Assuming the EC_{CO} (as derived in Sect. 4) do not change drastically over the years, we studied the entire time series and estimated CO emissions between 2003 and 2021 (see Fig. 9). As expected, the fire emissions from various regions around the globe have a high interannual variability. EURO and MIDE have the lowest emissions wildfire emissions for this entire time series, and cannot even be identified in the figure. The vast majority of wildfire CO emissions originate from SHAF and SHSA, followed by NHAF. It seems that between 2003 and

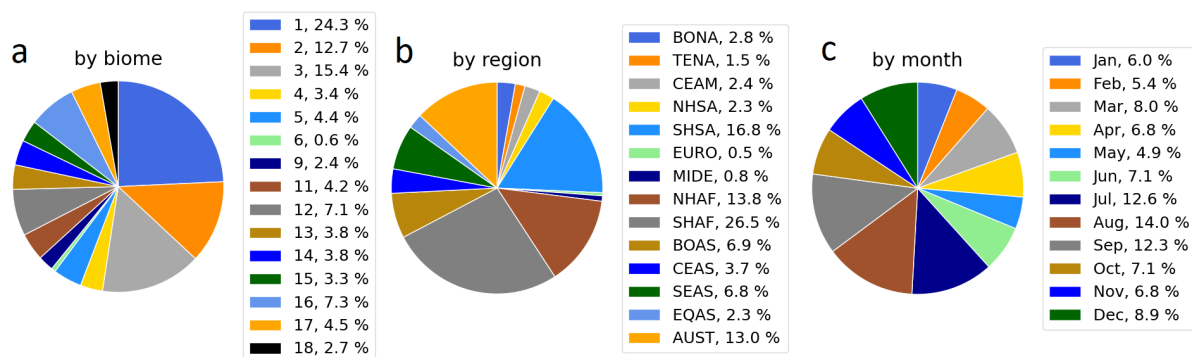


Figure 7. Analysis of the 2019 TROPOMI-FRE CO fire emissions: (a) emissions by different biomes as defined in Table B1, (b) by geographical regions as defined by Giglio et al. (2013)), (c) by month.

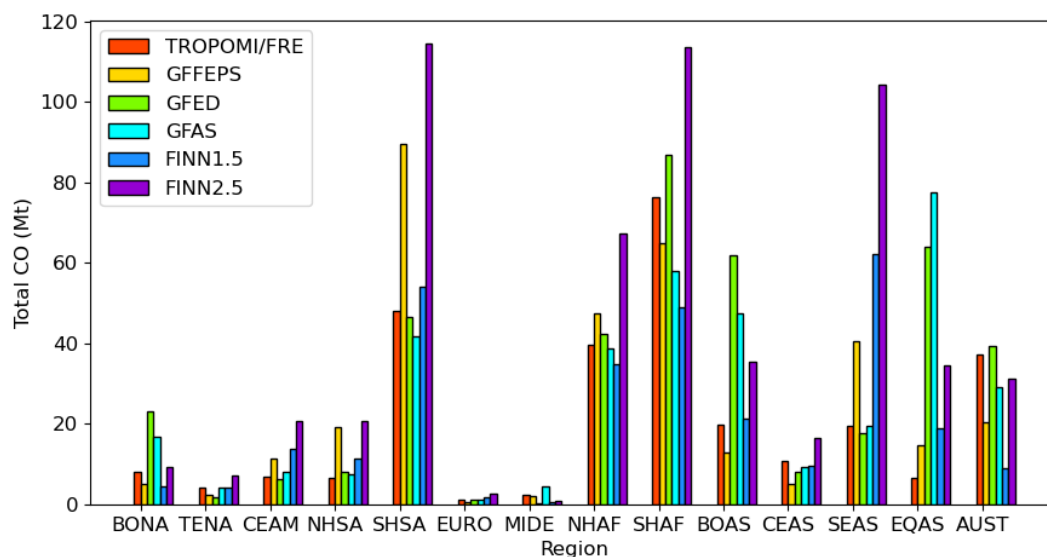


Figure 8. Comparison of total CO emissions from fires in 2019 for different fire emission inventories and TROPOMI-FRE for different geographical regions (as defined by Giglio et al. (2003)).

2021 the wildfire associated CO emissions are decreasing on a global scale, however, certain regions see increased emissions (e.g. TENA, AUST). Globally the emissions decrease during this time period, mainly driven by decreasing wildfire emissions in the highest emitting regions: SHAF, SHSA, and NHAF. These same figures have been created using GFED, GFAS CO, FINN v1.5 and v 2.5, and can be found in the Appendix D. Almost all of these also show a decrease of wildfire associated CO emissions globally during this time period, with the exception of GFED. In GFED, there seems to be a higher interannual

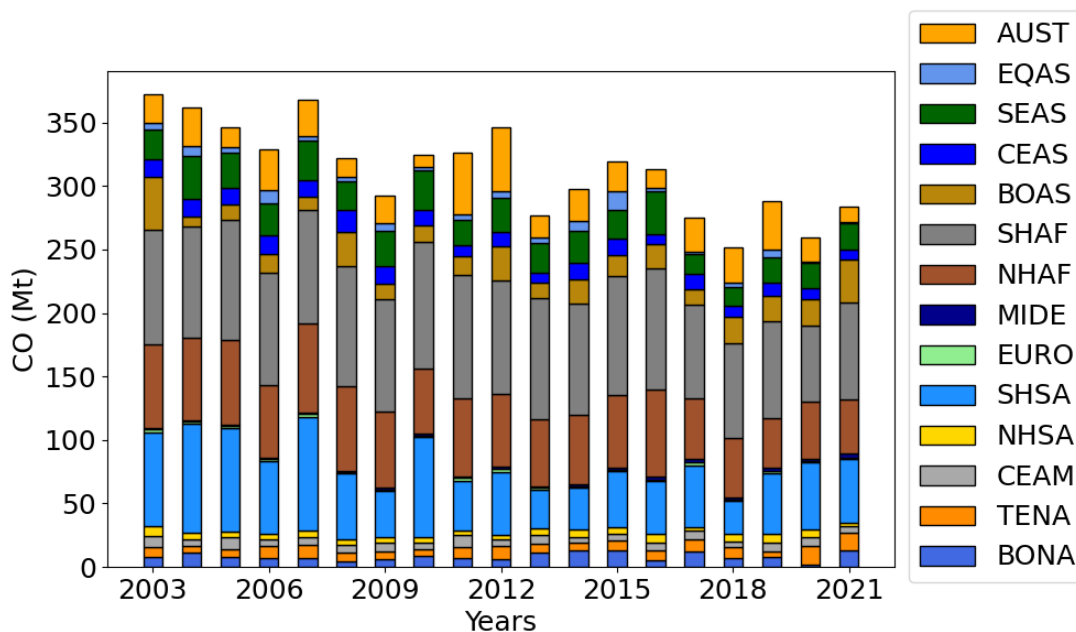


Figure 9. Total CO emissions from fires between 2003 and 2021 for different geographical regions (as defined by Giglio et al. (2003)) derived from GFAS FRP and TROPOMI-MODIS EC_{CO} (as defined in Table 2).

variability and peak CO emissions in 2015, 2019, and 2021 that are not as pronounced in the other emission inventories. These peaks are driven by high emissions in EQAS, AUST (and EQAS), and BOAS, respectively.

6 Conclusions

In this study, we presented an approach to compare TROPOMI-derived wildfire CO emissions with those from bottom-up and top-down emission inventories and emission prediction systems. Also highlighted is the importance of hotspots. When these are obscured, fire emissions cannot be estimated correctly with neither top-down or bottom-up that both rely on MODIS or VIIRS derived fire products. The directly-derived TROPOMI emission estimates are not impacted by this and have been used here to verify and analyse this issue for individual fires. With TROPOMI CO observations, wildfire emissions can be estimated from individual overpasses, resulting in roughly 5000 high quality fire emission estimates globally per year. The TROPOMI-derived CO estimates have precisely been validated with aircraft derived emission rates (Stockwell et al., 2022); here, we further established and automated an estimation method and performed model sensitivity tests to verify the robustness and uncertainties of the approach. Applying the same method to model VCDs, showed that the method is robust and is capable to derive the model input emissions when appropriate quality filters are applied. The success rate depends primarily on favorable meteorological conditions, including stable atmospheric conditions, low cloud and smoke cover, and no significant wind shear



465 in the area, as well as the proximity of other nearby sources (especially upwind). Applying appropriate filtering for unfavorable
wind conditions is the key for this method to work well and to reduce uncertainties of the emission estimates. The sensitivity
tests show that the methods uncertainty is approximately 42 %.

Further the TROPOMI-derived CO emissions have been used to obtain emission coefficients with respect to MODIS FRP.
470 This allows a method to determine a global CO emission budget to allow a comparison to other fire emission inventories, and
to determine total emissions and changes over time. TROPOMI alone cannot be used to study total emissions, as too many fires
are missed due to unfavorable meteorological conditions and the satellite is limited to a single daily overpass at 1:30pm. The
TROPOMI derived CO emissions have generally an average correlation with FRP ($R \sim 0.5 - 0.6$) for most biomes. Depending
on the biome different ECs have been derived with Tree cover, broadleaved, evergreen (biome type 1) showing the highest CO
475 emission relative to FRP. In this study we used the GLC2000 biome classification, and showed that there are large differences
of EC for different types of forests. Based on this analysis we would not recommend a more simplified classification (e.g. for
forests we determined ECs between 64 and 120 g/MJ), if anything the biomes could benefit from further distinction. We also
found that the FRP is strongly influenced by thick smoke which can influence these types of top-down emission estimates, and
leads to an underestimate of fire emissions for fires with thick smoke (typically large fires). This can explain to some extend
480 the outliers in the CO-FRP scatter plots. Differences between flaming and smoldering are also expected and will influence
the correlation between the CO emissions and FRP, however, it is very difficult to determine the burning stage especially on
a global scale for thousands of fires. When estimating the ECs the smoldering and flaming stages are neglected, though we
would expect that for a monthly or annual budget over different regions the effect will average out. There is much uncertainty
in this method as a single EC is assumed for each biome that is based on emission estimates at around 1:30pm local time. In
485 the near future geostationary satellites can be used to study total daily emissions and the ECs at different times of day.

In the comparison to GFFEPS, we identified the limitation to hotspot detection. GFFEPS relies on the satellite detected
hotspots, these feed directly into the estimate of burned area which is used to derive the bottom-up emissions. Thus, if not
all hotspots are captured the emissions will be underestimated. This discrepancy can be corrected for, but further analysis is
490 needed how exactly this can be accounted for.

The TROPOMI-FRP derived top-down emissions have been compared to other inventories. This comparison shows that
there are large discrepancies between different inventories, and highlights that fire emission inventories have large uncertain-
ties. GFFEPS tends to be closest to TROPOMI-FRE with the exception of some regions (SHSA, NHSA, SEAS, and AUST).
495 All these estimates are likely impacted by missing small fires, missing hotspots and an underestimation of FRP that ultimately
might lead to an underestimate of the total emissions. Over the last 20 years (lifetime of MODIS), global CO wildfire emissions
seem to decrease. This trend is due to the reduction of wildfire CO from the regions with the largest emissions (SHSA, NHAF,
SHAF), other regions (TENA, AUST, possibly BOAS) show increased wildfire CO emissions during this time period.



500 Overall, directly-derived TROPOMI CO emissions and CO VCD enhancements are a great tool for validation of fire emission models, e.g. GFFEPS. With this it was possible to pinpoint several issues, which either have been addressed or will be addressed in future versions of GFFEPS, such as the obstructed hotspots. Future geostationary satellite sensors, such as TEMPO (covering North America) or Sentinel-4 (covering Europe and Africa) will help to validate the diurnal pattern of emissions. WilfireSat (Johnston et al., 2020) will help with the FRP and hotspot count in the afternoon during the peak of the fire activity.



505 Appendix A: TROPOMI GFFEPS comparison

Table A1. TROPOMI-derived CO emissions versus GFFEPS CO emissions for different regions around the globe.

Region	Slope	R	RMSE	sample size
BONA	0.31	0.36	1976	183
TENA	0.42	0.51	1074	45
CEAM	1.80	0.59	401	22
NHSA	0.82	0.74	249	58
SHSA	0.42	0.33	844	789
EURO	0.20	0.44	215	7
MIDE	-0.60	-0.90	300	3
NHAF	0.19	0.31	446	557
SHAF	0.14	0.31	441	918
BOAS	0.35	0.56	895	403
CEAS	0.22	0.29	395	121
SEAS	0.33	0.07	579	203
EQAS	0.49	0.40	928	58
AUST	0.10	0.09	2986	672



Table A2. TROPOMI-derived CO emissions versus GFFEPS CO emissions for GLC2000 biomes (see Table B1 around the globe).

Fuel Type	Slope	R	RMSE	sample size
1	0.14	0.02	2794	706
2	0.14	0.23	866	356
3	0.25	0.41	885	768
4	0.47	0.44	1227	233
5	0.34	0.54	1008	248
6	0.32	0.77	1988	36
9	0.25	0.59	633	78
11	0.11	0.07	1545	150
12	0.40	0.53	444	519
13	0.25	0.34	640	193
14	0.61	0.35	395	172
15	0.25	0.37	564	85
16	0.46	0.34	199	131
17	0.32	0.40	806	166
18	0.12	0.73	1342	107



Appendix B: GLC2000

Table B1. GLC2000 biomes, see Bartholomé and Belward (2005).

Number	Description
1	Tree Cover, broadleaved, evergreen LCCS >15
2	Tree Cover, broadleaved, deciduous, closed
3	Tree Cover, broadleaved, deciduous, open
4	Tree Cover, needle-leaved, evergreen
5	Tree Cover, needle-leaved, deciduous
6	Tree Cover, mixed leaf type
7	Tree Cover, regularly flooded, fresh water
8	Tree Cover, regularly flooded, saline water
9	Mosaic: Tree cover / Other natural vegetation
10	Tree Cover, burnt
11	Shrub Cover, closed-open, evergreen
12	Shrub Cover, closed-open, deciduous
13	Herbaceous Cover, closed-open
14	Sparse Herbaceous or sparse Shrub Cover
15	Regularly flooded Shrub and/or Herbaceous Cover
16	Cultivated and managed areas
17	Mosaic: Cropland / Tree Cover / Other natural vegetation
18	Mosaic: Cropland / Shrub or Grass Cover
19	Bare Areas
20	Water Bodies (natural & artificial)
21	Snow and Ice (natural & artificial)
22	Artificial surfaces and associated areas

Appendix C: EC_{CO} for different years



Table C1. Same as Table 2, but for 2019 only. Note 2019 was the year of the “black summer” fires in Australia that burned mostly type 1 vegetation, those were extreme fires with very thick smoke.

Number	Description	EC _{CO} (g/MJ)	R	sample size	Rank
1	Tree Cover, broadleaved, evergreen	150	0.55	498	1
2	Tree Cover, broadleaved, deciduous, closed	100	0.61	194	4
3	Tree Cover, broadleaved, deciduous, open	53	0.71	357	2
4	Tree Cover, needle-leaved, evergreen	56	0.47	183	8
5	Tree Cover, needle-leaved, deciduous	111	0.47	220	10
6	Tree Cover, mixed leaf type	67	0.65	31	15
9	Mosaic: Tree cover / Other natural vegetation	72	0.82	44	12
11	Shrub Cover, closed-open, evergreen	100	0.78	89	13
12	Shrub Cover, closed-open, deciduous	28	0.37	220	3
13	Herbaceous Cover, closed-open	58	0.5	82	6
14	Sparse Herbaceous or sparse Shrub Cover	31	0.28	103	9
15	Regularly flooded Shrub and/or Herbaceous Cover	67	0.54	64	14
16	Cultivated and managed areas	28	0.36	62	5
17	Mosaic: Cropland / Tree Cover / Other natural vegetation	58	0.43	83	7
18	Mosaic: Cropland / Shrub or Grass Cover	69	0.46	60	11



Table C2. Same as Table 2, but for 2020 only.

Number	Description	EC_{CO} (g/MJ)	R	sample size	Rank
1	Tree Cover, broadleaved, evergreen	101	0.71	459	1
2	Tree Cover, broadleaved, deciduous, closed	93	0.57	225	4
3	Tree Cover, broadleaved, deciduous, open	79	0.42	346	2
4	Tree Cover, needle-leaved, evergreen	61	0.52	151	8
5	Tree Cover, needle-leaved, deciduous	90	0.43	294	10
6	Tree Cover, mixed leaf type	47	0.28	5	15
9	Mosaic: Tree cover / Other natural vegetation	67	0.22	47	12
11	Shrub Cover, closed-open, evergreen	75	0.26	103	13
12	Shrub Cover, closed-open, deciduous	43	0.76	227	3
13	Herbaceous Cover, closed-open	45	0.30	139	6
14	Sparse Herbaceous or sparse Shrub Cover	56	0.38	30	9
15	Regularly flooded Shrub and/or Herbaceous Cover	124	0.63	89	14
16	Cultivated and managed areas	38	0.67	146	5
17	Mosaic: Cropland / Tree Cover / Other natural vegetation	46	0.28	58	7
18	Mosaic: Cropland / Shrub or Grass Cover	50	0.34	56	11

Table C3. Same as Table 2, but for 2021 only.

Number	Description	EC_{CO} (g/MJ)	R	sample size	Rank
1	Tree Cover, broadleaved, evergreen	59	0.52	507	1
2	Tree Cover, broadleaved, deciduous, closed	42	0.30	252	4
3	Tree Cover, broadleaved, deciduous, open	28	0.22	439	2
4	Tree Cover, needle-leaved, evergreen	55	0.49	340	8
5	Tree Cover, needle-leaved, deciduous	92	0.30	915	10
6	Tree Cover, mixed leaf type	45	0.29	25	15
9	Mosaic: Tree cover / Other natural vegetation	65	0.69	75	12
11	Shrub Cover, closed-open, evergreen	123	0.53	101	13
12	Shrub Cover, closed-open, deciduous	34	0.43	295	3
13	Herbaceous Cover, closed-open	36	0.50	173	6
14	Sparse Herbaceous or sparse Shrub Cover	78	0.52	49	9
15	Regularly flooded Shrub and/or Herbaceous Cover	52	0.49	56	14
16	Cultivated and managed areas	94	0.60	130	5
17	Mosaic: Cropland / Tree Cover / Other natural vegetation	85	0.34	68	7
18	Mosaic: Cropland / Shrub or Grass Cover	63	0.88	87	11



Appendix D: CO emissions over the past two decades

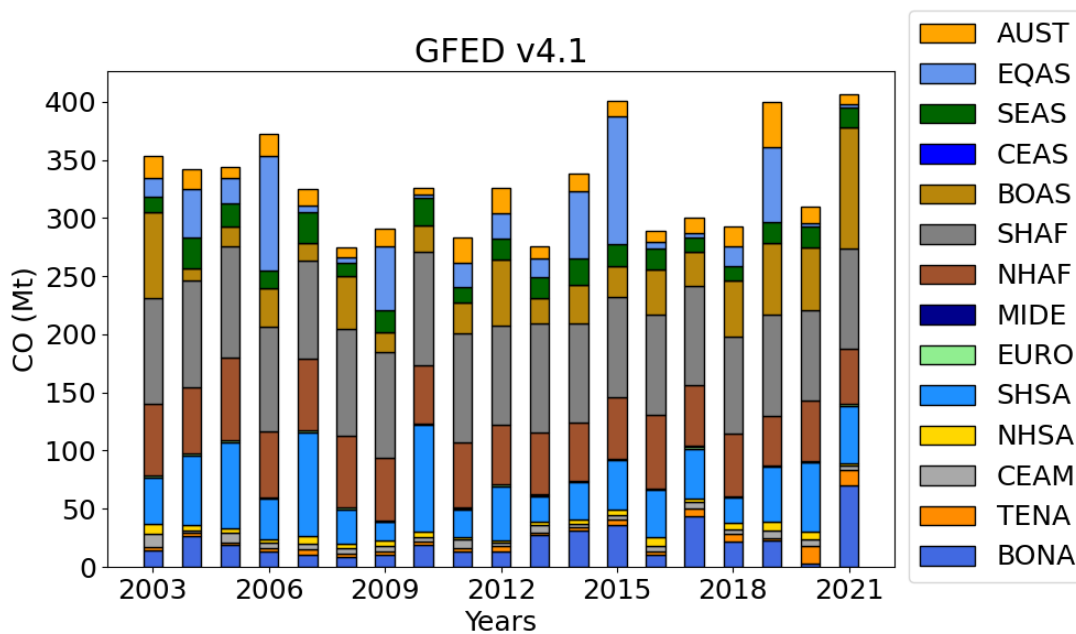


Figure D1. Same as Fig. 9 but for GFED v4.

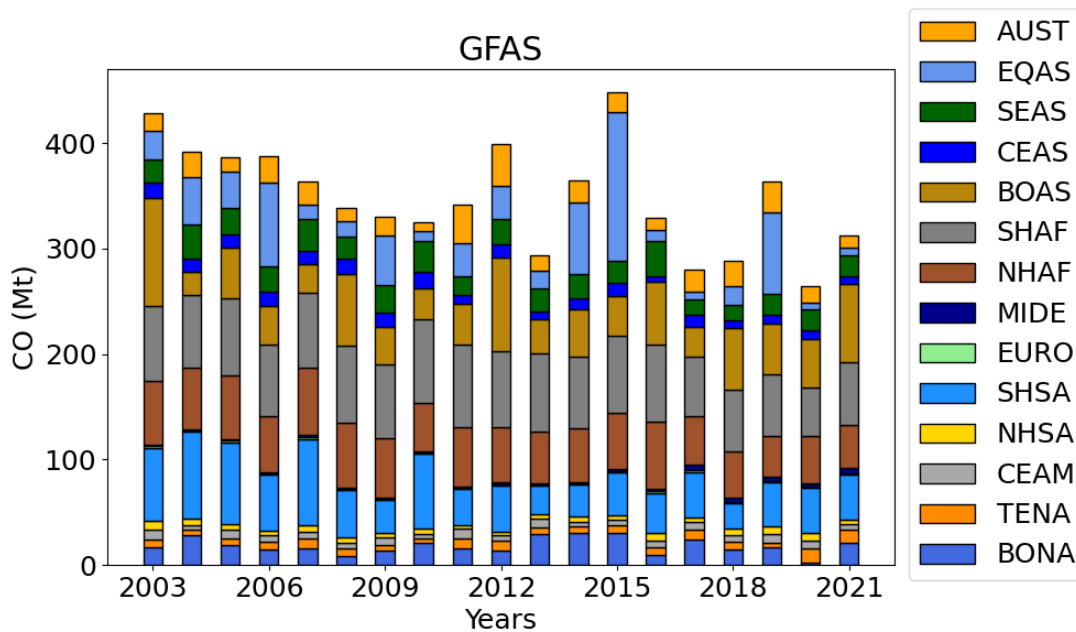


Figure D2. Same as Fig. 9 but for GFAS CO.

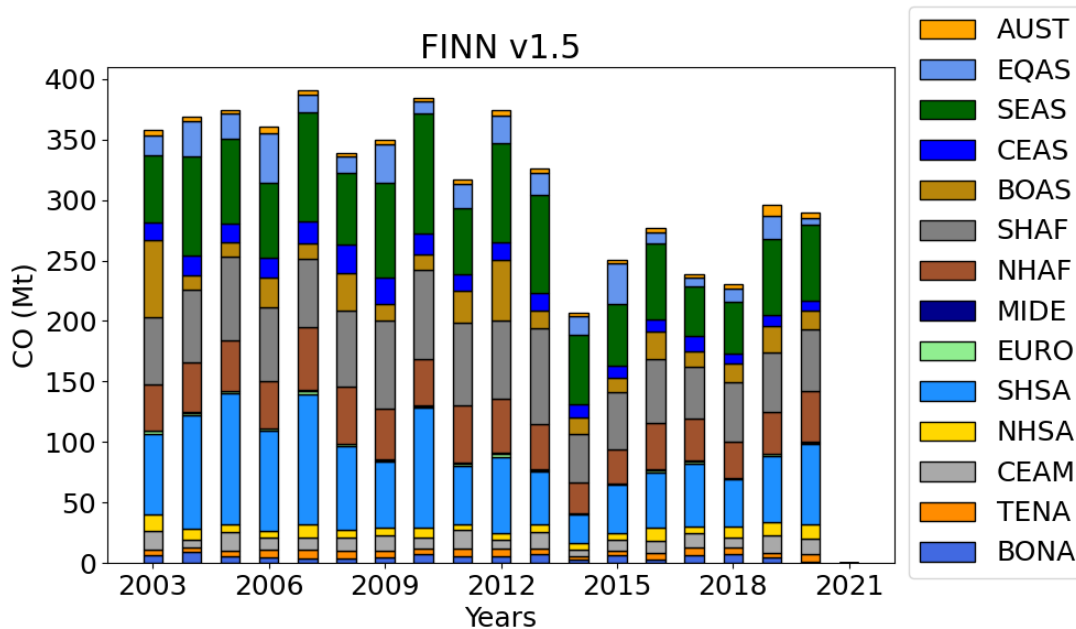


Figure D3. Same as Fig. 9 but for FINNv1.5.

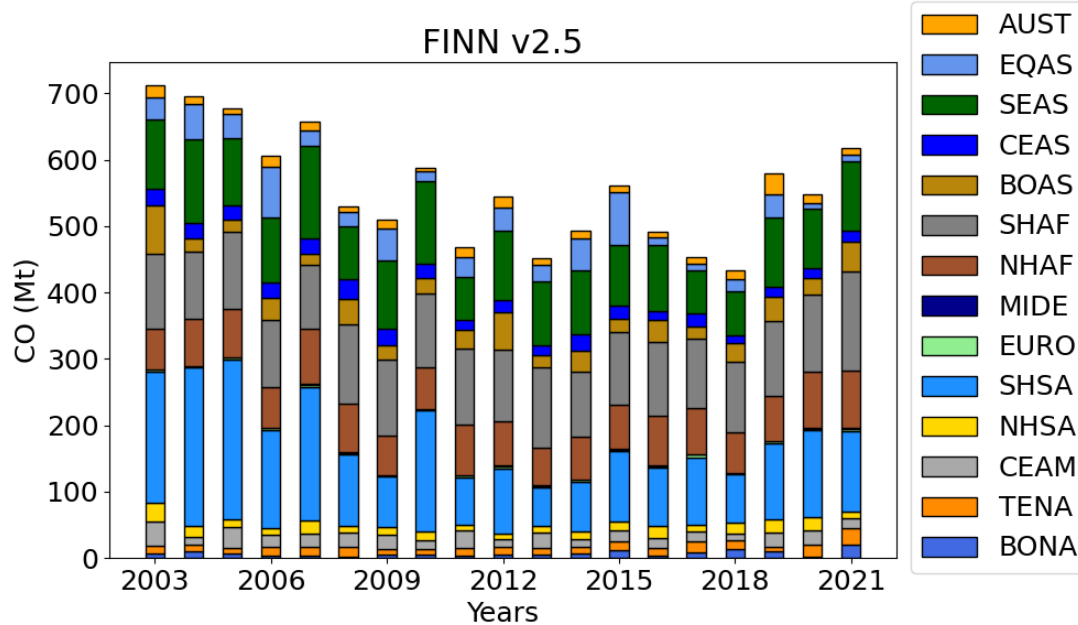


Figure D4. Same as Fig. 9 but for FINN v2.5.



510 *Data availability.* TROPOMI data can be downloaded from <https://s5phub.copernicus.eu>. The MODIS fire product is publicly available for download at: <http://modis-fire.umd.edu/index.php>.

Author contributions. DG, CAML, and ED developed the emissions estimation methods. KA, JC, and PM developed GFFEPS and prepared the GEM-MACH model run. AK and AF contributed to the data visualization. DG carried out the data analysis and prepared the article with contributions from all co-authors.

Competing interests. The authors declare no competing interests.

515 *Acknowledgements.* This work contains modified Copernicus Sentinel data. The Sentinel 5 Precursor TROPOMI Level 2 product is developed with funding from the Netherlands Space Office (NSO) and processed with funding from the European Space Agency (ESA). The MODIS data set was provided by LANCE FIRMS operated by NASA ESDIS with funding provided by NASA Headquarters. This study contains modified Copernicus Atmosphere Monitoring Service Information [2019]; neither the European Commission nor ECMWF is responsible for any use that may be made of the information it contains.



520 References

- Adams, C., McLinden, C. A., Shephard, M. W., Dickson, N., Dammers, E., Chen, J., Makar, P., Cady-Pereira, K. E., Tam, N., Kharol, S. K., Lamsal, L. N., and Krotkov, N. A.: Satellite-derived emissions of carbon monoxide, ammonia, and nitrogen dioxide from the 2016 Horse River wildfire in the Fort McMurray area, *Atmospheric Chemistry and Physics*, 19, 2577–2599, <https://doi.org/10.5194/acp-19-2577-2019>, 2019.
- 525 Andreae, M. O.: Emission of trace gases and aerosols from biomass burning – an updated assessment, *Atmospheric Chemistry and Physics*, 19, 8523–8546, <https://doi.org/10.5194/acp-19-8523-2019>, 2019.
- Apituley, A., Pedergnana, M., Sneep, M., Veefkind, J. P., Loyola, D., Landgraf, J., and Borsdorff, T.: Sentinel-5 precursor/TROPOMI Level 2 Product User Manual Carbon Monoxide, CI-7570-PUM, <https://sentinel.esa.int/documents/247904/2474726/Sentinel-5P-Level-2-Product-User-Manual-Carbon-Monoxide.pdf>, sRON-S5P-LEV2-MA-002, 2018.
- 530 Bartholomé, E. and Belward, A. S.: GLC2000: a new approach to global land cover mapping from Earth observation data, *International Journal of Remote Sensing*, 26, 1959–1977, <https://doi.org/10.1080/01431160412331291297>, 2005.
- Borsdorff, T., Aan de Brugh, J., Hu, H., Aben, I., Hasekamp, O., and Landgraf, J.: Measuring Carbon Monoxide With TROPOMI: First Results and a Comparison With ECMWF-IFS Analysis Data, *Geophysical Research Letters*, 45, 2826–2832, <https://doi.org/https://doi.org/10.1002/2018GL077045>, 2018.
- 535 Borsdorff, T., aan de Brugh, J., Schneider, A., Lorente, A., Birk, M., Wagner, G., Kivi, R., Hase, F., Feist, D. G., Sussmann, R., Rettinger, M., Wunch, D., Warneke, T., and Landgraf, J.: Improving the TROPOMI CO data product: update of the spectroscopic database and destriping of single orbits, *Atmospheric Measurement Techniques*, 12, 5443–5455, <https://doi.org/10.5194/amt-12-5443-2019>, 2019.
- Chen, J., Anderson, K., Pavlovic, R., Moran, M. D., Englefield, P., Thompson, D. K., Munoz-Alpizar, R., and Landry, H.: The FireWork v2.0 air quality forecast system with biomass burning emissions from the Canadian Forest Fire Emissions Prediction System v2.03, *Geoscientific Model Development*, 12, 3283–3310, <https://doi.org/10.5194/gmd-12-3283-2019>, 2019.
- 540 Clerbaux, C., Boynard, A., Clarisse, L., George, M., Hadji-Lazaro, J., Herbin, H., Hurtmans, D., Pommier, M., Razavi, A., Turquety, S., Wespes, C., and Coheur, P.-F.: Monitoring of atmospheric composition using the thermal infrared IASI/MetOp sounder, *Atmospheric Chemistry and Physics*, 9, 6041–6054, <https://doi.org/10.5194/acp-9-6041-2009>, 2009.
- Côté, J., Gravel, S., Méthot, A., Patoine, A., Roch, M., and Staniforth, A.: The Operational CMC–MRB Global Environmental Multiscale (GEM) Model. Part I: Design Considerations and Formulation, *Monthly Weather Review*, 126, 1373–1395, [https://doi.org/10.1175/1520-0493\(1998\)126<1373:TOCMGE>2.0.CO;2](https://doi.org/10.1175/1520-0493(1998)126<1373:TOCMGE>2.0.CO;2), 1998.
- 545 de Foy, B., Wilkins, J. L., Lu, Z., Streets, D. G., and Duncan, B. N.: Model evaluation of methods for estimating surface emissions and chemical lifetimes from satellite data, *Atmospheric Environment*, 98, 66 – 77, <https://doi.org/10.1016/j.atmosenv.2014.08.051>, 2014.
- Deeter, M. N., Martínez-Alonso, S., Edwards, D. P., Emmons, L. K., Gille, J. C., Worden, H. M., Pittman, J. V., Daube, B. C., and Wofsy, S. C.: 550 Validation of MOPITT Version 5 thermal-infrared, near-infrared, and multispectral carbon monoxide profile retrievals for 2000–2011, *Journal of Geophysical Research: Atmospheres*, 118, 6710–6725, <https://doi.org/https://doi.org/10.1002/jgrd.50272>, 2013.
- European Commission: Global Land Cover 2000 database, joint Research Centre; GLC 2000 [dataset], <https://forobs.jrc.ec.europa.eu/products/glc2000/products.php> [last accessed: 8 March 2023], 2003.
- Fathi, S., Gordon, M., Makar, P. A., Akingunola, A., Darlington, A., Liggio, J., Hayden, K., and Li, S.-M.: Evaluating the impact of storage-and-release on aircraft-based mass-balance methodology using a regional air-quality model, *Atmospheric Chemistry and Physics*, 21, 15 461–15 491, <https://doi.org/10.5194/acp-21-15461-2021>, 2021.



- Forestry Canada Fire Danger Group: Development and structure of the Canadian Forest Fire Behavior Prediction System. For Canada, Ottawa, Ont. Inf. Rep. ST-X-3. 63 p, 1992.
- 560 Giglio, L., Descloitres, J., Justice, C. O., and Kaufman, Y. J.: An Enhanced Contextual Fire Detection Algorithm for MODIS, *Remote Sensing of Environment*, 87, 273 – 282, [https://doi.org/10.1016/S0034-4257\(03\)00184-6](https://doi.org/10.1016/S0034-4257(03)00184-6), 2003.
- Giglio, L., Csaszar, I., and Justice, C. O.: Global distribution and seasonality of active fires as observed with the Terra and Aqua Moderate Resolution Imaging Spectroradiometer (MODIS) sensors, *Journal of Geophysical Research: Biogeosciences*, 111, <https://doi.org/10.1029/2005JG000142>, 2006.
- 565 Giglio, L., Randerson, J. T., and van der Werf, G. R.: Analysis of daily, monthly, and annual burned area using the fourth-generation global fire emissions database (GFED4), *Journal of Geophysical Research: Biogeosciences*, 118, 317–328, <https://doi.org/https://doi.org/10.1002/jgrg.20042>, 2013.
- Giglio, L., Schroeder, W., and Justice, C. O.: The collection 6 MODIS active fire detection algorithm and fire products, *Remote Sensing of Environment*, 178, 31 – 41, <https://doi.org/10.1016/j.rse.2016.02.054>, 2016.
- 570 Giglio, L., Boschetti, L., Roy, D., Hoffmann, A. A., and Humber, M.: Collection 6 MODIS Burned Area Product User’s Guide Version 1.3, *mCD64CMQ, Collection 6 [dataset]*, <https://ladsweb.modaps.eosdis.nasa.gov/missions-and-measurements/products/MCD64A1> [last accessed: 8 March 2023], 2020.
- Girard, C., Plante, A., Desgagné, M., McTaggart-Cowan, R., Côté, J., Charron, M., Gravel, S., Lee, V., Patoine, A., Qaddouri, A., Roch, M., Spacek, L., Tanguay, M., Vaillancourt, P. A., and Zadra, A.: Staggered Vertical Discretization of the Canadian Environmental Multiscale (GEM) Model Using a Coordinate of the Log-Hydrostatic-Pressure Type, *Monthly Weather Review*, 142, 1183–1196, <https://doi.org/10.1175/MWR-D-13-00255.1>, 2014.
- 575 Griffin, D., Zhao, X., McLinden, C. A., Boersma, F., Bourassa, A., Dammers, E., Degenstein, D., Eskes, H., Fehr, L., Fioletov, V., Hayden, K., Kharol, S. K., Li, S.-M., Makar, P., Martin, R. V., Mihele, C., Mittermeier, R. L., Krotkov, N., Sneep, M., Lamsal, L. N., Linden, M. t., Geffen, J. v., Veefkind, P., and Wolde, M.: High-Resolution Mapping of Nitrogen Dioxide With TROPOMI: First Results and Validation Over the Canadian Oil Sands, *Geophysical Research Letters*, 46, 1049–1060, <https://doi.org/10.1029/2018GL081095>, 2019.
- 580 Griffin, D., Sioris, C., Chen, J., Dickson, N., Kovachik, A., de Graaf, M., Nanda, S., Veefkind, P., Dammers, E., McLinden, C. A., Makar, P., and Akingunola, A.: The 2018 fire season in North America as seen by TROPOMI: aerosol layer height intercomparisons and evaluation of model-derived plume heights, *Atmospheric Measurement Techniques*, 13, 1427–1445, <https://doi.org/10.5194/amt-13-1427-2020>, 2020.
- Griffin, D., McLinden, C. A., Dammers, E., Adams, C., Stockwell, C. E., Warneke, C., Bourgeois, I., Peischl, J., Ryerson, T. B., Zarzana, K. J., Rowe, J. P., Volkamer, R., Knote, C., Kille, N., Koenig, T. K., Lee, C. F., Rollins, D., Rickly, P. S., Chen, J., Fehr, L., Bourassa, A., Degenstein, D., Hayden, K., Mihele, C., Wren, S. N., Liggio, J., Akingunola, A., and Makar, P.: Biomass burning nitrogen dioxide emissions derived from space with TROPOMI: methodology and validation, *Atmospheric Measurement Techniques*, 14, 7929–7957, <https://doi.org/10.5194/amt-14-7929-2021>, 2021.
- 585 Gualtieri, G.: Analysing the uncertainties of reanalysis data used for wind resource assessment: A critical review, *Renewable and Sustainable Energy Reviews*, 167, 112 741, <https://doi.org/https://doi.org/10.1016/j.rser.2022.112741>, 2022.
- 590 Guo, M., Li, J., Wen, L., and Huang, S.: Estimation of CO₂ Emissions from Wildfires Using OCO-2 Data, *Atmosphere*, 10, <https://doi.org/10.3390/atmos10100581>, 2019.
- Hayden, K., Li, S.-M., Liggio, J., Wheeler, M., Wentzell, J., Leithead, A., Brickell, P., Mittermeier, R., Oldham, Z., Mihele, C., Staebler, R., Moussa, S., Darlington, A., Steffen, A., Wolde, M., Thompson, D., Chen, J., Griffin, D., Eckert, E., Ditto, J., He, M., and Gentner, D.:



- Reconciling the total carbon budget for boreal forest wildfire emissions using airborne observations, *Atmospheric Chemistry and Physics*, 2022, 1–62, <https://doi.org/10.5194/acp-2022-245>, 2022.
- 595 Hu, H., Landgraf, J., Detmers, R., Borsdorff, T., de Brugh, J. A., Aben, I., Butz, A., and Hasekamp, O.: Toward Global Mapping of Methane With TROPOMI: First Results and Intersatellite Comparison to GOSAT, *Geophysical Research Letters*, 45, 3682–3689, <https://doi.org/10.1002/2018GL077259>, 2018.
- Jin, X., Zhu, Q., and Cohen, R. C.: Direct estimates of biomass burning NO_x emissions and lifetimes using daily observations from TROPOMI, *Atmospheric Chemistry and Physics*, 21, 15 569–15 587, <https://doi.org/10.5194/acp-21-15569-2021>, 2021.
- 600 Johnston, J. M., Jackson, N., McFayden, C., Ngo Phong, L., Lawrence, B., Davignon, D., Wooster, M. J., van Mierlo, H., Thompson, D. K., Cantin, A. S., Johnston, D., Johnston, L. M., Sloane, M., Ramos, R., and Lynham, T. J.: Development of the User Requirements for the Canadian WildFireSat Satellite Mission, *Sensors*, 20, <https://doi.org/10.3390/s20185081>, 2020.
- Kaiser, J. W., Heil, A., Andreae, M. O., Benedetti, A., Chubarova, N., Jones, L., Morcrette, J.-J., Razinger, M., Schultz, M. G., Suttie, M., and van der Werf, G. R.: Biomass burning emissions estimated with a global fire assimilation system based on observed fire radiative power, *Biogeosciences*, 9, 527–554, <https://doi.org/10.5194/bg-9-527-2012>, 2012.
- 605 Kaufman, Y. J., Justice, C. O., Flynn, L. P., Kendall, J. D., Prins, E. M., Giglio, L., Ward, D. E., Menzel, W. P., and Setzer, A. W.: Potential global fire monitoring from EOS-MODIS, *Journal of Geophysical Research: Atmospheres*, 103, 32 215–32 238, <https://doi.org/10.1029/98JD01644>, 1998.
- 610 Landis, M. S., Edgerton, E. S., White, E. M., Wentworth, G. R., Sullivan, A. P., and Dillner, A. M.: The impact of the 2016 Fort McMurray Horse River Wildfire on ambient air pollution levels in the Athabasca Oil Sands Region, Alberta, Canada, *Science of The Total Environment*, 618, 1665 – 1676, <https://doi.org/10.1016/j.scitotenv.2017.10.008>, 2018.
- Lee, B. S., Alexander, M. E., Hawkes, B. C., Lynham, T. J., Stocks, B. J., and Englefield, P.: Information systems in support of wildland fire management decision making in Canada, *Computers and Electronics in Agriculture*, 37, 185–198, 2002.
- 615 Littell, J. S., McKenzie, D., Peterson, D. L., and Westerling, A. L.: Climate and wildfire area burned in western U.S. ecoprovinces, 1916–2003, *Ecological Applications*, 19, 1003–1021, <https://doi.org/10.1890/07-1183.1>, 2009.
- Liu, Y., Goodrick, S. L., and Stanturf, J. A.: Future U.S. wildfire potential trends projected using a dynamically downscaled climate change scenario, *Forest Ecology and Management*, 294, 120 – 135, <https://doi.org/10.1016/j.foreco.2012.06.049>, 2013.
- Makar, P., Gong, W., Hogrefe, C., Zhang, Y., Curci, G., Žabkar, R., Milbrandt, J., Im, U., Balzarini, A., Baró, R., Bianconi, R., Cheung, P., Forkel, R., Gravel, S., Hirtl, M., Honzak, L., Hou, A., Jiménez-Guerrero, P., Langer, M., Moran, M., Pabla, B., Pérez, J., Pirovano, G., José, R. S., Tuccella, P., Werhahn, J., Zhang, J., and Galmarini, S.: Feedbacks between air pollution and weather, part 2: Effects on chemistry, *Atmospheric Environment*, 115, 499 – 526, <https://doi.org/10.1016/j.atmosenv.2014.10.021>, 2015a.
- 620 Makar, P., Gong, W. F., Milbrandt, J., Hogrefe, C., Zhang, Y., Curci, G., Žabkar, R., Im, U., Balzarini, A., Baró, R., Bianconi, R., Cheung, P., Forkel, R., Gravel, S., Hirtl, M., Honzak, L., Hou, A., Jimenez-Guerrero, P., Langer, M., and Galmarini, S.: Feedbacks between air pollution and weather, Part 1: Effects on weather, *Atmospheric Environment*, 115, <https://doi.org/10.1016/j.atmosenv.2014.12.003>, 2015b.
- 625 Makar, P. A., Akingunola, A., Chen, J., Pabla, B., Gong, W., Stroud, C., Sioris, C., Anderson, K., Cheung, P., Zhang, J., and Milbrandt, J.: Forest Fire Aerosol – Weather Feedbacks over Western North America Using a High-Resolution, Fully Coupled, Air-Quality Model, *Atmospheric Chemistry and Physics Discussions*, 2020, 1–55, <https://doi.org/10.5194/acp-2020-938>, 2020.
- Martínez-Alonso, S., Deeter, M., Worden, H., Borsdorff, T., Aben, I., Commane, R., Daube, B., Francis, G., George, M., Landgraf, J., 630 Mao, D., McKain, K., and Wofsy, S.: 1.5 years of TROPOMI CO measurements: comparisons to MOPITT and ATom, *Atmospheric Measurement Techniques*, 13, 4841–4864, <https://doi.org/10.5194/amt-13-4841-2020>, 2020.



- Matz, C. J., Egyed, M., Xi, G., Racine, J., Pavlovic, R., Rittmaster, R., Henderson, S. B., and Stieb, D. M.: Health impact analysis of PM_{2.5} from wildfire smoke in Canada (2013–2015, 2017–2018), *Science of The Total Environment*, 725, 138506, <https://doi.org/10.1016/j.scitotenv.2020.138506>, 2020.
- 635 Mebust, A. K. and Cohen, R. C.: Space-based observations of fire NO_x emission coefficients: a global biome-scale comparison, *Atmospheric Chemistry and Physics*, 14, 2509–2524, <https://doi.org/10.5194/acp-14-2509-2014>, 2014.
- Mebust, A. K., Russell, A. R., Hudman, R. C., Valin, L. C., and Cohen, R. C.: Characterization of wildfire NO_x emissions using MODIS fire radiative power and OMI tropospheric NO₂ columns, *Atmospheric Chemistry and Physics*, 11, 5839–5851, <https://doi.org/10.5194/acp-11-5839-2011>, 2011.
- 640 Meng, J., Martin, R. V., Li, C., van Donkelaar, A., Tzompa-Sosa, Z. A., Yue, X., Xu, J.-W., Weagle, C. L., and Burnett, R. T.: Source Contributions to Ambient Fine Particulate Matter for Canada, *Environmental Science & Technology*, 53, <https://doi.org/10.1021/acs.est.9b02461>, 2019.
- Pope, R. J., Kerridge, B. J., Siddans, R., Latter, B. G., Chipperfield, M. P., Arnold, S. R., Ventress, L. J., Pimlott, M. A., Graham, A. M., Knappe, D. S., and Rigby, R.: Large Enhancements in Southern Hemisphere Satellite-Observed Trace Gases Due to the 2019/2020 Australian Wildfires, *Journal of Geophysical Research: Atmospheres*, 126, e2021JD034892, <https://doi.org/https://doi.org/10.1029/2021JD034892>, 2021.
- 645 Romero-Lankao, P., Smith, J. B., Davidson, D. J., Diffenbaugh, N. S., Kinney, P. L., Kirshen, P., Kovacs, P., and Villers Ruiz, L.: *Climate Change 2014: Impacts, Adaptation, and Vulnerability. Part B: Regional Aspects, Contribution of Working Group II to the Fifth Assessment Report of the Intergovernmental Panel on Climate Change*, Cambridge University Press, Cambridge, UK and New York, NY, USA, 2014.
- 650 Schneising, O., Buchwitz, M., Reuter, M., Bovensmann, H., and Burrows, J. P.: Severe Californian wildfires in November 2018 observed from space: the carbon monoxide perspective, *Atmospheric Chemistry and Physics*, 20, 3317–3332, <https://doi.org/10.5194/acp-20-3317-2020>, 2020.
- Sha, M. K., Langerock, B., Blavier, J.-F. L., Blumenstock, T., Borsdorff, T., Buschmann, M., Dehn, A., De Mazière, M., Deutscher, N. M., Feist, D. G., García, O. E., Griffith, D. W. T., Grutter, M., Hannigan, J. W., Hase, F., Heikkinen, P., Hermans, C., Iraci, L. T., Jeseck, P., Jones, N., Kivi, R., Kumps, N., Landgraf, J., Lorente, A., Mahieu, E., Makarova, M. V., Mellqvist, J., Metzger, J.-M., Morino, I., Nagahama, T., Notholt, J., Ohyama, H., Ortega, I., Palm, M., Petri, C., Pollard, D. F., Rettinger, M., Robinson, J., Roche, S., Roehl, C. M., Röhling, A. N., Rousogonous, C., Schneider, M., Shiomi, K., Smale, D., Stremme, W., Strong, K., Sussmann, R., Té, Y., Uchino, O., Velazco, V. A., Vigouroux, C., Vrekoussis, M., Wang, P., Warneke, T., Wizenberg, T., Wunch, D., Yamanouchi, S., Yang, Y., and Zhou, M.: Validation of methane and carbon monoxide from Sentinel-5 Precursor using TCCON and NDACC-IRWG stations, *Atmospheric Measurement Techniques*, 14, 6249–6304, <https://doi.org/10.5194/amt-14-6249-2021>, 2021.
- 660 Stocks, B., Lawson, B., Alexander, M., Wagner, C., McAlpine, R., Lynham, T., and Dube, D.: The Canadian forest fire danger rating system: an overview, *The Forestry Chronicle*, 65, 450–457, <https://doi.org/10.5558/tfc65450-6>, 1989.
- Stockwell, C. E., Bela, M. M., Coggon, M. M., Gkatzelis, G. I., Wiggins, E., Gargulinski, E. M., Shingler, T., Fenn, M., Griffin, D., Holmes, C. D., Ye, X., Saide, P. E., Bourgeois, I., Peischl, J., Womack, C. C., Washenfelder, R. A., Veres, P. R., Neuman, J. A., Gilman, J. B., 665 Lamplugh, A., Schwantes, R. H., McKeen, S. A., Wisthaler, A., Piel, F., Guo, H., Campuzano-Jost, P., Jimenez, J. L., Fried, A., Hanisco, T. F., Huey, L. G., Perring, A., Katich, J. M., Diskin, G. S., Nowak, J. B., Bui, T. P., Halliday, H. S., DiGangi, J. P., Pereira, G., James, E. P., Ahmadov, R., McLinden, C. A., Soja, A. J., Moore, R. H., Hair, J. W., and Warneke, C.: Airborne Emission Rate Measurements Validate Remote Sensing Observations and Emission Inventories of Western U.S. Wildfires, *Environmental Science & Technology*, 56, 7564–7577, <https://doi.org/10.1021/acs.est.1c07121>, 2022.



- 670 Urbanski, S.: Wildland fire emissions, carbon, and climate: Emission factors, *Forest Ecology and Management*, 317, 51–60, <https://doi.org/10.1016/j.foreco.2013.05.045>, 2014.
- van der Velde, I., van der Werf, G., Houweling, S., Maasakkers, J., Borsdorff, T., Landgraf, J., Tol, P., van Krempen, T.A., van Hees, R., Hoogeveen, R., Veefkind, J., and Aben, I.: Vast CO₂ release from Australian fires in 2019–2020 constrained by satellite, *Nature*, 597, 366–369, <https://doi.org/https://doi.org/10.1038/s41586-021-03712-y>, 2021.
- 675 van der Werf, G. R., Randerson, J. T., Giglio, L., van Leeuwen, T. T., Chen, Y., Rogers, B. M., Mu, M., van Marle, M. J. E., Morton, D. C., Collatz, G. J., Yokelson, R. J., and Kasibhatla, P. S.: Global fire emissions estimates during 1997–2016, *Earth System Science Data*, 9, 697–720, <https://doi.org/10.5194/essd-9-697-2017>, 2017.
- van Leeuwen, T. T., van der Werf, G. R., Hoffmann, A. A., Detmers, R. G., Rücker, G., French, N. H. F., Archibald, S., Carvalho Jr., J. A., Cook, G. D., de Groot, W. J., Hély, C., Kasischke, E. S., Kloster, S., McCarty, J. L., Pettinari, M. L., Savadogo, P., Alvarado, E. C.,
- 680 Boschetti, L., Manuri, S., Meyer, C. P., Siegert, F., Trollope, L. A., and Trollope, W. S. W.: Biomass burning fuel consumption rates: a field measurement database, *Biogeosciences*, 11, 7305–7329, <https://doi.org/10.5194/bg-11-7305-2014>, 2014.
- van Wagner, C. E.: Development and structure of the Canadian Forest Fire Weather Index System, Canadian Forestry Service Headquarters, Forestry Tech. Rep., <https://cfs.nrcan.gc.ca/pubwarehouse/pdfs/19927.pdf>, 1987.
- Veefkind, J., Aben, I., McMullan, K., Forster, H., de Vries, J., Otter, G., Claas, J., Eskes, H., de Haan, J., Kleipool, Q., van Weele, M.,
- 685 Hasekamp, O., Hoogeveen, R., Landgraf, J., Snel, R., Tol, P., Ingmann, P., Voors, R., Kruizinga, B., Vink, R., Visser, H., and Levelt, P.: TROPOMI on the ESA Sentinel-5 Precursor: A GMES mission for global observations of the atmospheric composition for climate, air quality and ozone layer applications, *Remote Sensing of Environment*, 120, 70 – 83, <https://doi.org/10.1016/j.rse.2011.09.027>, the Sentinel Missions - New Opportunities for Science, 2012.
- Warneke, C., Schwarz, J. P., Dibb, J., Kalashnikova, O., Frost, G., Al-Saad, J., Brown, S. S., Brewer, W. A., Soja, A., Seidel, F. C., Washenfelder, R. A., Wiggins, E. B., Moore, R. H., Anderson, B. E., Jordan, C., Yacovitch, T. I., Herndon, S. C., Liu, S., Kuwayama, T., Jaffe, D., Johnston, N., Selimovic, V., Yokelson, R., Giles, D. M., Holben, B. N., Goloub, P., Popovici, I., Trainer, M., Kumar, A., Pierce, R. B., Fahey, D., Roberts, J., Gargulinski, E. M., Peterson, D. A., Ye, X., Thapa, L. H., Saide, P. E., Fite, C. H., Holmes, C. D., Wang, S., Coggon, M. M., Decker, Z. C. J., Stockwell, C. E., Xu, L., Gkatzelis, G., Aikin, K., Lefer, B., Kaspari, J., Griffin, D., Zeng, L., Weber, R., Hastings, M., Chai, J., Wolfe, G. M., Hanisco, T. F., Liao, J., Campuzano Jost, P., Guo, H., Jimenez, J. L., Crawford, J., and Team, T. F.-A. S.:
- 695 Fire Influence on Regional to Global Environments and Air Quality (FIREX-AQ), *Journal of Geophysical Research: Atmospheres*, 128, e2022JD037758, <https://doi.org/https://doi.org/10.1029/2022JD037758>, e2022JD037758 2022JD037758, 2023.
- Westerling, A. L.: Increasing western US forest wildfire activity: sensitivity to changes in the timing of spring, *Philosophical Transactions of the Royal Society B: Biological Sciences*, 371, 20150178, <https://doi.org/10.1098/rstb.2015.0178>, 2016.
- Wiedinmyer, C., Akagi, S. K., Yokelson, R. J., Emmons, L. K., Al-Saadi, J. A., Orlando, J. J., and Soja, A. J.: The Fire INventory from
- 700 NCAR (FINN): a high resolution global model to estimate the emissions from open burning, *Geoscientific Model Development*, 4, 625–641, <https://doi.org/10.5194/gmd-4-625-2011>, 2011.
- Wooster, M. J., Roberts, G., Perry, G. L. W., and Kaufman, Y. J.: Retrieval of biomass combustion rates and totals from fire radiative power observations: FRP derivation and calibration relationships between biomass consumption and fire radiative energy release, *Journal of Geophysical Research: Atmospheres*, 110, <https://doi.org/10.1029/2005JD006318>, 2005.
- 705 Wotton, B. M., Flannigan, M. D., and Marshall, G. A.: Potential climate change impacts on fire intensity and key wildfire suppression thresholds in Canada, *Environmental Research Letters*, 12, 095003, <https://doi.org/10.1088/1748-9326/aa7e6e>, 2017.

<https://doi.org/10.5194/egusphere-2023-649>

Preprint. Discussion started: 10 May 2023

© Author(s) 2023. CC BY 4.0 License.



Yue, X., Mickley, L. J., Logan, J. A., Hudman, R. C., Martin, M. V., and Yantosca, R. M.: Impact of 2050 climate change on North American wildfire: consequences for ozone air quality, *Atmospheric Chemistry and Physics*, 15, 10033–10055, <https://doi.org/10.5194/acp-15-10033-2015>, 2015.